Dissociative recombination and low-energy inelastic electron collisions of the helium dimer ion

H. B. Pedersen,[1,*] H. Buhr,[1] S. Altevogt,[1] V. Andrianarijaona,[1] H. Kreckel,[1] L. Lammich,[1] N. de Ruette,[2]
E. M. Staicu-Casagrande,[2] D. Schwalm,[1] D. Strasser,[3] X. Urbain,[2] D. Zajfman,[1,3] and A. Wolf[1]

[1]*Max-Planck-Institut für Kernphysik, D-69117 Heidelberg, Germany*
[2]*Département de Physique, Université Catholique de Louvain, B-1348, Louvain-la-Neuve, Belgium*
[3]*Department of Particle Physics, Weizmann Institute of Science, Rehovot 76100, Israel*
(Received 23 November 2004; published 15 July 2005)

The dissociative recombination (DR) of ^{3}He ^{4}He$^+$ has been investigated at the heavy-ion Test Storage Ring (TSR) in Heidelberg by observing neutral products from electron-ion collisions in a merged beams configuration at relative energies from near-zero (thermal electron energy about 10 meV) up to 40 eV. After storage and electron cooling for 35 s, an effective DR rate coefficient at near-zero energy of 3×10^{-9} cm^{3}s^{-1} is found. The temporal evolution of the neutral product rates and fragment imaging spectra reveals that the populations of vibrational levels in the stored ion beam are nonthermal with fractions of ~0.1–1 % in excited levels up to at least $v=4$, having a significant effect on the observed DR signals. With a pump-probe-type technique using DR fragment imaging while switching the properties of the electron beam, the vibrational excitation of the ions is found to originate mostly from ion collisions with the residual gas. Also, the temporal evolution of the DR signals suggests that a strong electron induced rotational cooling occurs in the vibrational ground state, reaching a rotational temperature near or below 300 K. From the absolute rate coefficient and the shape of the fragment imaging spectrum observed under stationary conditions, the DR rate coefficient from the vibrational ground state is determined; converted to a thermal electron gas at 300 K it amounts to $(3.3 \pm 0.9) \times 10^{-10}$ cm^{3}s^{-1}. The corresponding branching ratios from $v=0$ to the atomic final states are found to be (3.7 ± 1.2) % for $1s2s \, ^3S$, (37.4 ± 4.0) % for $1s2s \, ^1S$, (58.6 ± 5.2) % for $1s2p \, ^3P$, and (2.9 ± 3.0) % for $1s2p \, ^1P$. A DR rate coefficient in the range of 2×10^{-7} cm^{3}s^{-1} or above is inferred for vibrational levels $v=3$ and higher. As a function of the collision energy, the measured DR rate coefficient displays a structure around 0.2 eV. At higher energies, it has one smooth peak around 7.3 eV and a highly structured appearance at 15–40 eV. The small size of the observed effective DR rate coefficient at near-zero energy indicates that the electron induced rotational cooling is due to inelastic electron-ion collisions and not due to selective depletion of rotational levels by DR.

I. INTRODUCTION

Low-energy collisions of diatomic, positive molecular ions with free electrons are important processes in cold dilute media, such as the interstellar medium, planetary atmospheres, and laboratory discharges where they are among the reactions controlling the degree of ionization and the chemical composition. Usually the dominant neutralization process is the dissociative recombination (DR) [1] between an incident molecular ion AB^+ and a free electron e^-,

$$AB^+(v,J) + e^-(E) \rightarrow A(n) + B(n'), \qquad (1)$$
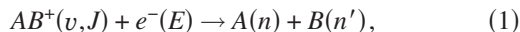
where v and J denote the rovibrational quantum numbers of the molecular ion, while E and n, n' are the electron energy and the atomic final-state quantum numbers, respectively. Beside recombination, dissociative reactions with charged products exist, which are represented by

$$AB^+(v,J) + e^-(E) \rightarrow \begin{Bmatrix} A^+(n) + B(n') \\ A(n) + B^+(n') \end{Bmatrix} + e^-(E') \qquad (2)$$
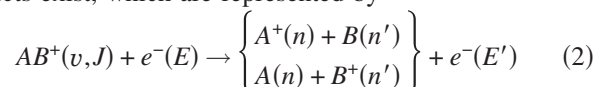
and termed dissociative excitation (DE). Finally, nondissociative inelastic interactions occur, in particular through collisions of the type

$$AB^+(v,J) + e^-(E) \rightarrow AB^+(v',J') + e^-(E'), \qquad (3)$$
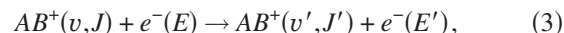
which describe the electron-impact excitation or de-excitation of nuclear motion in the molecular ion.

Beyond the relevance of these collision processes in cold dilute media, the understanding of their underlying quantum dynamical mechanisms is of fundamental interest. In particular, nonadiabatic dynamics manifestly violating the Born-Oppenheimer approximation often plays an important role, which makes low-energy electron collisions of small molecular ions a benchmark case for understanding nonadiabatic molecular interactions involving electronic continuum states.

For DR, the attractive interaction in the initial state and the exothermic, nonradiative nature of the process mostly lead to large cross sections at low collision energies, often reaching the order of 10^{-14} cm^2 for an incident energy of $E \sim 0.03$ eV. For many systems, including the experimentally and theoretically well studied cases of H$_2^+$ and its isotopomers [2] as well as heavier systems such as O$_2^+$ [3,4], NO$^+$ [5,6], and others, a slow incident electron can be resonantly captured by purely electronic interactions into doubly excited repulsive states of the neutral system, which enables the "direct" mechanism [1,7] as an efficient pathway for DR. Some systems exist where suitable electronic potentials for the direct process are absent for the low-lying rovibrational states;

*Author to whom correspondence should be addressed. Electronic address: henrik.pedersen@mpi-hd.mpg.de
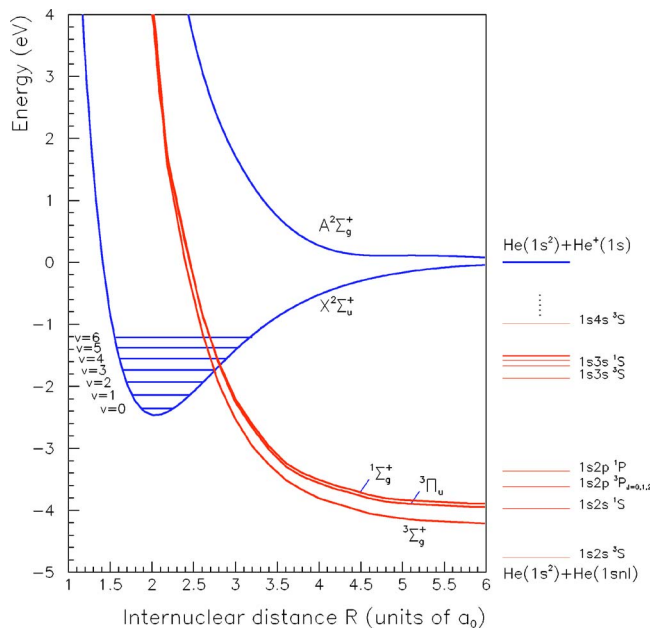
FIG. 1. (Color online) Potential-energy curves for the $X\,^2\Sigma_u^+$ electronic ground state of He_2^+ [20] and its first dissociative state ($A\,^2\Sigma_g^+$) [21] together with the three lowest dissociating curves of He_2 [10,28]. The energetic positions of the first seven vibrational levels of $^3He\,^4He^+$ are shown as horizontal lines in the $X\,^2\Sigma_u^+$ potential. Asymptotically, the $^3\Sigma_g^+$ state correlates to $He(1s^2\,^1S)$ $+He(1s2s\,^3S)$, the $^1\Sigma_g^+$ state to $He(1s^2\,^1S)+He(1s2s\,^1S)$, and the $^3\Pi_u$ state to $He(1s^2\,^1S)+He(1s2p\,^3P)$.

however, in many such cases, including the astrophysically important molecular ions HeH^+ and H_3^+ [2], nonadiabatic mechanisms are nevertheless considered to cause DR with similar cross sections as in the direct process [1,8].

A system falling outside this picture is the helium dimer ion, He_2^+. From early theoretical work [9] up to the most recent calculation [10], extremely low cross sections (of order 10^{-18} cm^2 for $E\sim0.03$ eV) have been predicted for the DR of He_2^+ in low-lying initial vibrational states. Electronic potential curves driving the direct DR process at low electron energies are not accessible from the lower vibrational states, as shown in Fig. 1. The inclusion of rovibrational interactions in theoretical calculations [10] causes a rich structure of narrow electron capture resonances, but still yields a small effect in the energy-averaged rate coefficient; these calculations did not include nonadiabatic coupling to neutral states below the ion curve as a significant increase of the cross section because such coupling was not expected. For excited vibrational states ($v\gtrsim3$), much larger DR cross sections ($\sim10^{-14}$ cm^2 at $E\sim0.03$ eV as typical for other species) are predicted [10]. The low-energy DR of helium dimer ions should therefore be characterized by extreme variations of the cross sections among the low vibrational states.

The helium dimer ion is of importance in models of the early universe [11] and in laboratory plasmas. Particularly, He_2^+ is the dominant ion in the fundamental helium plasmas and in the helium afterglow at pressures above ~5 mbar [12] and at room temperature (while atomic ions dominate the low-pressure He afterglows or at higher temperature). In the helium plasma, He_2^+ is created in either three-body [13] or

binary collisions [12,14] giving ions with a significant rovibrational excitation [12,15]. The helium afterglow is characterized by a strong recombination of electrons and molecular ions and the simultaneous occurrence of excited (triplet) helium atoms [16]. The DR of He_2^+ ions was suggested early on [7] to explain the observed recombination [17]. However, later experiments and modeling suggested collisional-radiative recombination ($He_2^+ + 2e^- \rightarrow He_2^* + e^-$) as the dominent process, with the DR rate coefficient being negligible at an upper limit of $<5\times10^{-10}$ cm^3/s [12]. DR from higher vibrational states (certainly present in the studied high-pressure afterglows) was also argued to be negligible, while other studies of the He afterglow and plasma [18,19] showed a significant role of DR for vibrationally excited ions in producing excited He atoms with $n=3$, 4. Thus the actual role of DR in high-pressure He afterglows remains unclear.

The structure of the He_2^+ ion is well studied theoretically [20,21] and several experimental studies were peformed [22–27]. In particular, the precise data from vibrational spectroscopy [24] and the high-level calculations on the electronic potential-energy surface for He_2^+ make it possible to calculate accurate nuclear wave functions, reliable vibrational and rotational radiative lifetimes, and accurate kinetic energy releases for the DR process, all of which are essential to interpret the experimental results presented in this paper.

Regarding the low-energy DR process, already Mulliken [9], on the basis of qualitative arguments on the electronic structure of He_2, suggested that the rate from the vibrational ground states of He_2^+ should be very small, while still significant for higher vibrational levels. Calculated diabatic potential-energy curves for dissociative states by Cohen [28] and Guberman [29] confirmed this hypothesis, since no curve crossing exists close to the ground vibrational state of the ion and the dissociative curves of the neutral, thus suppressing the direct route of DR. In a recent paper Carata *et al.* [10] presented multichannel quantum defect theory (MQDT) calculations on the low-energy DR of He_2^+ addressing several aspects of importance for an experimental study. For the three isotopomers, the DR from the vibrational states $v=0-4$ was calculated (including also rotational excitation) considering the lowest three neutral dissociative curves of the symmetries $^3\Sigma_g^+$, $^1\Sigma_g^+$, and $^3\Pi_u$ with the diabatic asymptotic limits of $He(1s^2\,^1S)$ $+He(1s2s\,^3S), He(1s^2\,^1S)+He(1s2s\,^1S)$, and $He(1s^2\,^1S)$ $+He(1s2p\,^3P)$, respectively (see Fig. 1). At low relative energies (0–0.1 eV) and for $v=0-2$, the $^3\Sigma_g^+$ curve was found to provide the dominant dissociation route, with a very small cross section ranging from $\sim10^{-18}-10^{-16}$ cm^2 for $v=0$, leading to a rate coefficient of only 6.1×10^{-11} cm^3/s at 300 K. Oppositely, for $v=3$ and 4 the preferred dissociation route was found to be $^3\Pi_u$ with an average cross section about four orders of magnitude larger than for $v=0$. Also the rotational excitation was found to influence the DR cross section, the result increasing by about a factor of 2 in going from $J=0$ to $J=9$ for $^3He\,^4He^+$ ($v=0$). In the work of Carata *et al.* [10] curve crossing in the asymptotic region was not explicitly considered and therefore the branching ratios into the final channels were not predicted, however, it was argued that dissociation should preferentially proceed on the dominant
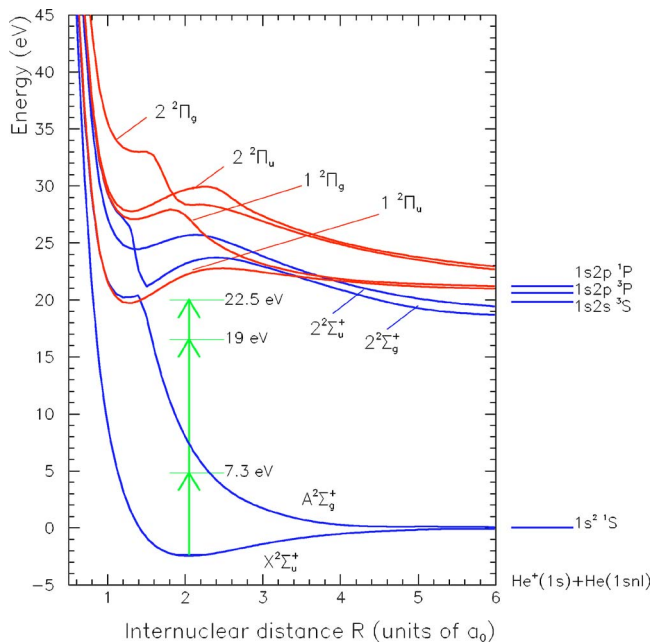
FIG. 2. (Color online) The lowest doublet potential-energy curves of the He_2^+ system as calculated by Ackermann and Hogreve [21]. The vertical arrows indicate the energetic positions above the vibrational ground state of ^3He $^4He^+$ where major structures in the DR rate coefficient have been observed in the present measurement.

dissociative curve for a given vibrational level ($^3\Sigma_g^+$ for v =0–2).

Regarding DR at higher electron energies, the available detailed calculations for excited electronic states of He_2^+ [21] indicate at which energies and internuclear distances doubly excited neutral states, suitable for resonant electron capture and subsequent dissociation, could be expected. An overview of the predicted higher-lying potential curves of He_2^+ are given in Fig. 2. Rydberg-like doubly excited neutral states can occur in energy regions extending down by $\sim$3 eV from the calculated excited ionic potential curves. Considering the Franck-Condon zone of He_2^+ (v=0), peaks in the DR rate due to resonant electron capture are expected and in fact observed in the data presented here at electron energies of $\sim$6–10 eV and further up at $\gtrsim$20 eV.

In the present experiment, DR and other related electron-induced reactions are studied for the asymmetric isotopomer ^3He $^4He^+$ of the helium dimer ion, using a stored ion beam and a merged cold electron beam at the heavy-ion Test Storage Ring (TSR) in Heidelberg [30]. The extreme variation of the DR cross section with the vibrational quantum number imposes large demands on the understanding of the ion-beam evolution during the experiment. In particular, the predicted difference in the average DR cross section of four orders of magnitude [10] in going from v=0 to v=3 makes the experimental DR techniques sensitive to a population of vibrationally excited states of $\lesssim10^{-4}$ in the ion beam.

This sensitivity was already noted in the only earlier merged beams experiment on the DR of He_2^+, performed by Urbain *et al.* [31] at the ASTRID storage ring using ^3He $^4He^+$ and ^4He $^4He^+$. The results for the two species differed strongly from each other, as expected from their differ-

ent infrared emission properties in the case of a strong initial vibrational excitation. For ^4He $^4He^+$, a DR cross section monotonously decreasing with the collision energy was observed between 0 and 15 eV with no time dependence over $\sim$14 s of storage time, while the ^3He $^4He^+$ DR cross section showed a peak at around 6 eV and a strong decrease with time in the low-energy region. Thus a high sensitivity of the reaction rate to the internal excitation, with a small cross section for lower vibrational states, was demonstrated.

In order to extract quantitative information on the DR process and related low-energy electron collisions of He_2^+, a major part of the present experimental work is devoted to clarifying the internal excitation dynamics of an electron cooled ^3He $^4He^+$ ion beam in a storage ring. On the one hand, the Coulomb explosion imaging technique (Sec. III) is used to monitor the vibrational population of the stored ion beam while, on the other hand, time-dependent measurements of DR rate coefficients (Sec. IV A) and DR fragment imaging distributions (Sec. IV B) are employed as diagnostic tools to understand the evolution of the distribution of rovibrational states in the stored ion beam.

Measurements over long ion storage times (up to 70 s) reveal a dependence of the low-energy DR rate on the rotational excitation of the ^3He $^4He^+$ beam and indicate internal cooling of the stored ion beam by rotationally inelastic electron collisions (Sec. V A).

Time-dependent observations of structures in the DR fragment imaging distributions (Sec. V B) and pump-probe-type experiments (Sec. V C) serve to identify the vibrational levels contributing to the measured signal; in addition, they are used to measure the variation of electron-impact vibrational excitation rates of ^3He $^4He^+$ in an electron energy range of 2–9 eV.

After identifying these contributions, the branching ratios for the final atomic states (Sec. VI A) and the absolute low-energy DR rate coefficient (Sec. VI B) are extracted for ^3He $^4He^+$ (v=0) ions. Energy-dependent absolute cross sections are obtained for low-energy DR (Sec. VI C) and for high-energy DR and DE (Sec. VI D and VI E). Finally, the results on DR are considered in the light of previous experimental and theoretical data (Sec. VII A) and the cross sections of vibrationally and rotationally inelastic collisions, as implied by the present data, are discussed (Sec. VII B).

Using the same arrangement and similar procedures, measurements have also been performed on ^4He $^4He^+$; these results will be presented in a forthcoming publication.

II. EXPERIMENTAL BACKGROUND

A. Ion-beam and detector setup

The experiment was conducted at the Test Storage Ring (TSR) [30] at the Max-Planck-Institut für Kernphysik in Heidelberg. A schematic drawing of the experimental setup is displayed in Fig. 3. The basic experimental procedures have been described in detail earlier regarding merged electron and ion-beam experiments in general [32], DR of molecular ions [33,34], and Coulomb explosion imaging [35,36].
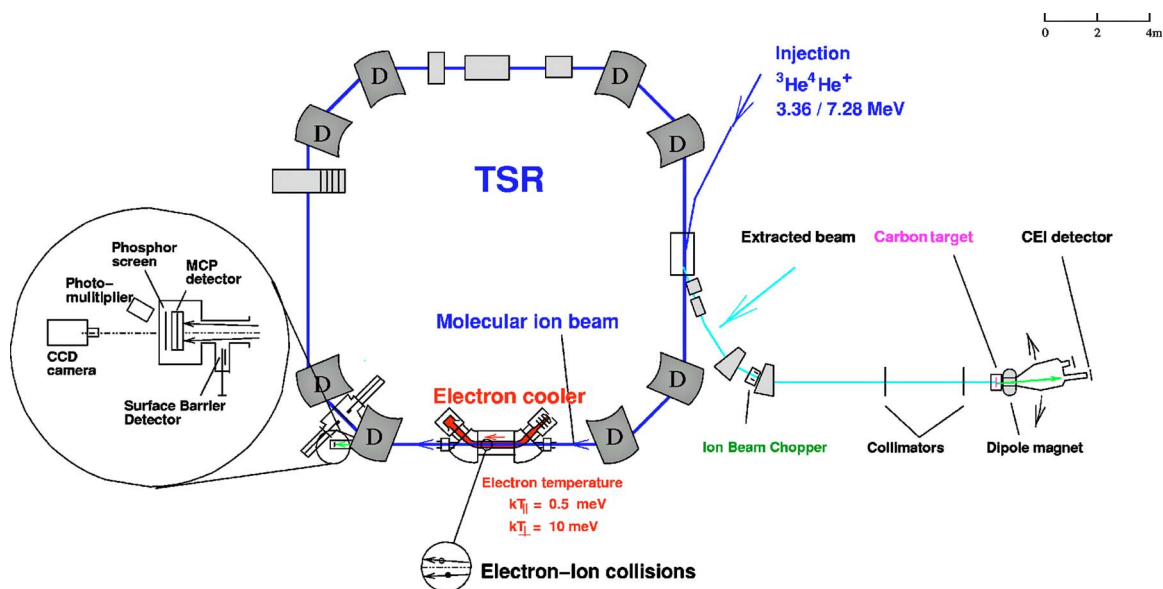
FIG. 3. (Color online) Schematic drawing of the experimental setup around the TSR.

For the present experiment, helium dimer ions were produced in a standard duoplasmatron ion source [37]. Ion source geometries both with and without an expansion cup following the anode were tested. Without an expansion cup the source delivered 300–500 nA of ^{3}He ^{4}He$^+$ for total pressures of 0.4–1.1 mbar in the filament chamber and an arc current of 0.33 down to 0.08 mA. The currents of atomic ^{3}He$^+$ and ^{4}He$^+$ were kept about equal at 20–30 μA. With an expansion cup in the ion source, the absolute yields of ^{3}He ^{4}He$^+$ were considerably lower and the source showed less stable operation. During the measurements reported here we used the source geometry without expansion cup, keeping the pressure in the cathode chamber at 0.6 mbar and the arc current close to 0.10 mA. Weak amounts of N^{2+} were observed in the beam with the Coulomb explosion technique (Sec. III). In all the experiments performed in this work small traces of N^{2+} in the beam have no influence on the results.

The ions were accelerated to kinetic energies E_i of either 7.28 or 3.36 MeV using an rf accelerator [38,39], transported to the storage ring by means of several magnetic steering and focusing elements, injected into the storage ring and stored in the field of its bending and focusing magnets. Pulses of a few nA were injected for about 150 μs and the ions were stored for times up to 70 s with a mean lifetime $(1/e)$ of 9.8 s. The beam loss is mainly determined by ion collisions with species of the residual gas which is composed mostly $(\geq 90\%)$ of H$_2$. The average pressure in the storage ring was 5–10×10^{-11} mbar during the present measurements.

The TSR electron cooler [40,41] was used to apply phase-space cooling to the stored He$_2^+$ ion beam [42] and to perform the electron-ion recombination experiments [32,33]. The electron beam is guided by a longitudinal magnetic field $(\sim 0.04$ T) and has a diameter of 29.5 mm in the region where the electron and ion beam overlap collinearly, surrounded by a 1.5-m-long solenoid magnet. In two toroid magnets adjacent to the "central" region of the electron

cooler, the electron beam is bent in and out of the overlap region. Neutral products created by interactions of the He$_2^+$ ions in the straight section of the storage ring containing the electron cooler are separated from the circulating ion beam at the downstream storage-ring magnet (see Fig. 3) and detected behind this magnet as described in detail below.

The relative velocity of electrons and ions in the central part of the electron cooler is controlled by the electron acceleration voltage [32]. The difference between the average longitudinal ion and electron velocities defines the detuning velocity v_d and the corresponding detuning energy $E_d = (m/2)v_d^2$ (where m denotes the electron mass, which here in good approximation can be used to replace the reduced mass). The collision velocities **v** are distributed according to an anisotropic Maxwellian [32] characterized by the electron temperatures $T_\perp$ and $T_\parallel$ perpendicular and parallel to the beam direction, respectively. For the present experiment $kT_\perp = 10$ meV and $kT_\parallel = 0.5$ meV.

The average beam velocities can be exactly matched $(E_d = 0)$ choosing a laboratory electron energy $E_e^c = (m/M)E_i$ (M denoting the ion mass). At this setting, called the "cooling" energy, efficient translational (phase-space) cooling of the stored ion beam takes place through Coulomb scattering [42] between the ions and the colder and continuously renewed electrons. The time needed for completion of the phase-space cooling depends on the initial ion temperature, the electron intensity, and the detailed injection conditions; for the present measurements the phase-space cooling was completed after 6 s, at the latest. For energy-dependent studies of electron-ion interactions, the laboratory electron energy E_e can be detuned from E_e^c, yielding finite detuning energies E_d for the relative motion between electrons and ions, as further discussed in Sec. IV A.

At velocity matching $(E_d = 0)$, electrons and ions interact with typical collision energies E in the 10-meV range, corresponding to the transverse electron temperature $(kT_\perp)$. At an ion energy of $E_i = 7.28$ MeV, the cooling energy of the

electron beam was $E_e^c = 571$ eV and electron densities n_e of 1.2×10^7 cm^{-3} and 5.5×10^6 cm^{-3} were used, as specified below. At $E_i = 3.36$ MeV, the cooling energy was $E_e^c = 263$ eV and the electron density was 5.5×10^6 cm^{-3}.

Applying electron energies $E_e > E_e^c$, relative energies E_d up to ~ 50 eV were adjusted, resulting in electron collision energies with a full width at half maximum (FWHM) spread [32] of, e.g., ~ 0.2 eV at $E_d = 10$ eV. Variations of E_d are connected with slight but significant variations of electron density $n_e(E_d)$.

Two types of detectors are used behind the storage-ring dipole magnet (Fig. 3) to count and analyze the neutral products created by interactions of the ^{3}He ^{4}He$^+$ ions with the merged electron beam or with residual gas molecules. An energy-sensitive surface barrier detector with a size of 40 $\times$ 60 mm^2, centered to the beam axis, served to count and discriminate events with neutral products. With essentially unit efficiency, each event creates an output pulse of this detector whose height is proportional to the total kinetic energy of all neutral products. As all neutral products propagate with the ion-beam velocity, the pulse height thus represents the total mass of neutral fragments, corresponding to 3, 4, or 7 atomic mass units (amu) if a single ^{3}He atom, a single ^{4}He atom, or two (^{3}He$+^4$He) atoms arrive in the neutral product channel. The interpretation of the corresponding, mass-discriminated neutral count rates $R_{(3)}, R_{(4)}$, and $R_{(7)}$ in terms of rate coefficients for electron and residual gas induced processes will be discussed below.

Instead of the surface barrier detector, also a multiparticle imaging detector [33] could be used in the detector chamber. From an 80-mm-diameter multichannel plate, equipped with a phosphor screen, the transverse coordinates of all fragments arriving within a coincidence time window of a few microseconds is read out with an event-triggered camera system. This system is used for DR fragment imaging as described in Sec. IV B.

B. Event rates for electron-induced processes

The elementary rate coefficient $\alpha_X(E_d)$ of any electron-induced process X, as represented by Eqs. (1)–(3), is related to the cross section $\sigma_X(E)$ of this process for a given collision energy $E = (m/2)\mathbf{v}^2$ through the average over the electron velocity distribution according to

$$\alpha_X(E_d) = \int |\mathbf{v}| \sigma_X(E) f(v_d, \mathbf{v}) d^3v, \tag{4}$$

where $f(v_d, \mathbf{v})$ is the electron velocity distribution [32] at a given detuning velocity $v_d = (2E_d/m)^{1/2}$. In the present work it will be important for some of the electron-induced processes to consider the dependence of their rate on the rovibrational state v, J of the stored molecular ions. In this context, the ensemble of N_i stored ions will be described by normalized populations $p_{vJ}(t)$ in the various rovibrational levels, which in general can depend on the storage time (time since injection) t. Introducing state-dependent elementary rate coefficients $\alpha_X(E_d) \equiv \alpha_X^{vJ}(E_d)$ the observed rate coefficients will be the rovibrationally averaged quantities

$$\widetilde{\alpha}_X(E_d) = \sum_{vJ} p_{vJ}(t) \alpha_X^{vJ}(E_d). \tag{5}$$

Using these rate coefficients, the rate R_X of an electron-induced process X occurring in the central overlap region of the electron cooler can be written as

$$R_X = \eta N_i n_e(E_d) \widetilde{\alpha}_X(E_d). \tag{6}$$

Here, $\eta = L/C$, where L is the length of the central overlap region (1.5 m in the present experiment) and C is the storage ring circumference (55.4 m, yielding $\eta = 0.027$). The expression given in Eq. (6) is not complete, as additional electron-induced reactions occur in the toroid regions where the electron beam, over a part of its bent section, still overlaps the ion beam. In contrast to the central region, where a single controlled value of E_d occurs, the detuning energy in the toroid regions rises fast as a consequence of the rapidly increasing angle between the two beams [33,43]. In the present measurements, the beams still overlap on a length of ~ 16 cm in each of the bends adjacent to the central section, and the excess detuning energy in these regions rises by up to ~ 10 eV. The rate R_X will hence include an additional toroid contribution $\widetilde{\alpha}_X^{\mathrm{tor}}(E_d)$, so that Eq. (6) should be replaced by

$$R_X = \eta N_i n_e(E_d) \left[\widetilde{\alpha}_X(E_d) + \widetilde{\alpha}_X^{\mathrm{tor}}(E_d) \right]. \tag{7}$$

with [34,43]

$$\widetilde{\alpha}_X^{\mathrm{tor}}(E_d) = \frac{2}{L} \int_{x_{\min}}^{x_{\max}} \widetilde{\alpha}_X(\widetilde{E}_d(x; E_d)) dx. \tag{8}$$

Here, $\widetilde{E}_d(x; E_d)$ denotes the shifted detuning energy as a function of the longitudinal position x in the toroid region, obtained from the known beam geometry. From an energy-dependent rate measurement $R_X(E_d)$ covering a suitably wide range of detuning energies E_d it is possible to obtain the toroid contribution $\widetilde{\alpha}_X^{\mathrm{tor}}(E_d)$ and hence the corrected rate coefficient $\widetilde{\alpha}_X(E_d)$ through a robust iterative procedure [34,43].
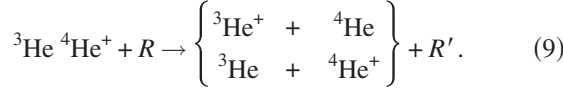
C. Stored ion-beam evolution

Understanding the temporal evolution of the rovibrational level distribution in the stored and electron cooled ion beam is essential for the interpretation of the experimental results presented. Hence in this section we outline and model the main processes that lead to beam loss and influence the rovibrational populations. In particular, the rovibrational states are coupled to the ~ 300-K blackbody radiation field in the storage ring. Moreover, the stored ions experience collisions with electrons in the electron cooler and with species in the residual gas leading to loss, excitation, and de-excitation of vibrational and rotational motion. To serve in the discussion of experimental data, expressions for the time dependence of the stored ion number, the neutral fragment count rates, and the rovibrational populations will be derived.

1. Beam loss and neutral fragment count rates

The relevant processes leading to ion loss from the circulating beam are inelastic collisions with residual gas mol-

ecules and with electrons in the electron cooler. Beam loss through elastic scattering processes can be neglected. In collisions with a residual gas particle (R), the dominant loss arises through the DE-type reactions,

$$^3\text{He} \, ^4\text{He}^+ + R \rightarrow \begin{Bmatrix} ^3\text{He}^+ & + & ^4\text{He} \\ ^3\text{He} & + & ^4\text{He}^+ \end{Bmatrix} + R'. \quad (9)$$

For each of these processes we define a rate constant k_{DE}^g, which describes the reaction rate per stored ion and depends on the reaction cross section and the gas density. Residual gas collsions can also lead to dissociative charge exchange (DC),

$$^3\text{He} \, ^4\text{He}^+ + R \rightarrow \, ^3\text{He} + \, ^4\text{He} + R', \quad (10)$$
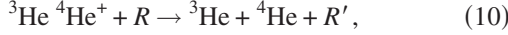
described by the rate constant k_{DC}^g. At the MeV ion-beam energies used here, it is expected that $k_{\text{DC}}^g \ll k_{\text{DE}}^g$; also, we assume for simplicity that at these collision energies both k_{DE}^g and k_{DC}^g are independent of the initial rovibrational state of the molecular ion. The rate constant k_X^g for any rest-gas induced process X is related to the collision cross section σ_X^g by

$$k_X^g = n_g v_i \sigma_X^g, \quad (11)$$

where n_g ($\sim 10^6$ cm^{-3} in the present experiments) is the residual gas density.

The rovibrationally averaged rate constants of electron-induced reactions follow from Eq. (7) as

$$\tilde{k}_X(E_d;t) = \eta n_e \left[\tilde{\alpha}_X(E_d) + \tilde{\alpha}_X^{\text{tor}}(E_d) \right]. \quad (12)$$

Rate constants $k_X^{vJ}(E_d)$ for electron-induced reactions on ions in a specific rovibrational level are defined in a similar manner. The loss of ions from the circulating beam is then described by the following rate equation for the ion number N_i:

$$\dot{N}_i = - \left[2k_{\text{DE}}^g + k_{\text{DC}}^g + \tilde{k}_{\text{DR}}(E_d;t) + 2\tilde{k}_{\text{DE}}(E_d;t) \right] N_i, \quad (13)$$

where rate constants for the electron-induced DR and DE reactions were introduced.

Similarly, the count rates representing the arrival of one or the correlated arrival of two neutral particles at the surface barrier detector (see Sec. II A) can be described; the properties of this detector allow unit counting efficiency to be assumed. For events yielding two neutrals ($^3\text{He} + \, ^4\text{He}$) the rate is given by

$$R_{(7)} = \left[f_g k_{\text{DC}}^g + \tilde{k}_{\text{DR}}(E_d;t) \right] N_i, \quad (14)$$

while the rates for the observation of a single neutral fragment(^3He or ^4He) are given by

$$R_{(3)} = R_{(4)} = \left[f_g k_{\text{DE}}^g + \tilde{k}_{\text{DE}}(E_d;t) \right] N_i. \quad (15)$$

Here f_g is a geometrical factor expressing the fraction of all residual gas events (which occur over all the ring circumference) that leads to a neutral particle detection on the surface barrier detector.

2. Radiative thermalization

Since the $^3\text{He} \, ^4\text{He}^+$ molecular ions have a permanent electrical dipole moment, their rovibrational motion is coupled to
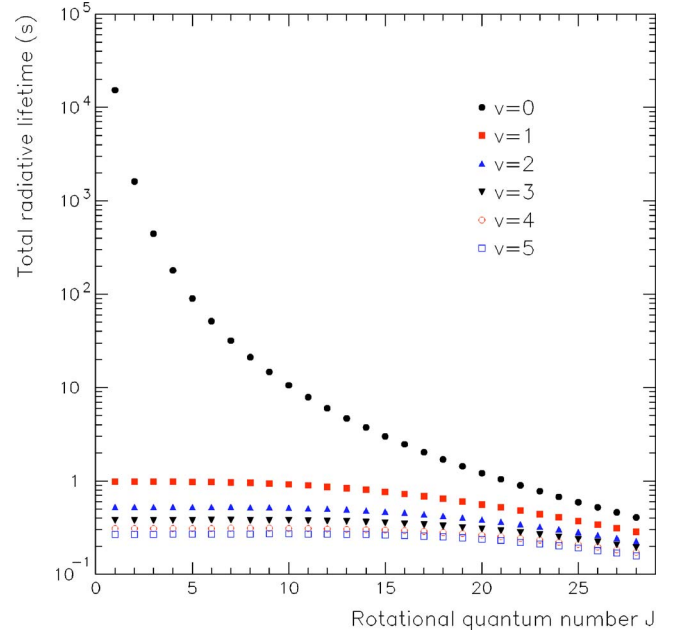

FIG. 4. (Color online) Calculated total radiative lifetimes as a function of the rotational quantum number J for the first six vibrational levels ($v=0$–5) in the $X\,^2\Sigma_u^+$ electronic ground state of $^3\text{He}\,^4\text{He}^+$.

the 300-K radiation field of the storage ring. Based on the potential–energy curve [20] for the $X\,^2\Sigma_u^+$ electronic ground state of He$_2^+$ we have calculated the Einstein coefficients for spontaneous emission(A_f^i), stimulated emission (S_f^i), and absorption (B_f^i) for rovibrational transitions connecting initial (i) and final (f) rovibrational levels; the same approach and approximations as in Ref. [44] were used [45]. Since the spin-rotational interaction is negligible, the rotational quantum numbers are $J=0, 1, 2,\ldots$ and the line strengths for $^1\Sigma - ^1\Sigma$ transitions have been used instead of those for $^2\Sigma - ^2\Sigma$ transitions [46], with the selection rule $\Delta J = \pm 1$. Figure 4 shows the results of these calculations for the total radiative lifetime $\tau_{vJ} = 1/\Sigma_{(v'J')<(vJ)} A_{v'J'}^{vJ}$, as a function of rotational quantum number J for the first six vibrational states of the $^2\Sigma_u^+$ ground state of $^3\text{He}\,^4\text{He}^+$. [The notations $(v'J')<(vJ)$ and $(v'J')>(vJ)$ are used to label the levels lying energetically below and above a given level vJ, respectively.]

The master equations for the numbers N_{vJ} of stored ions in states vJ under the influence of blackbody-induced radiative transitions are given by

$$\dot{N}_{vJ} = \sum_{(v'J')>(vJ)} \left\{ \left[A_{vJ}^{v'J'} + S_{vJ}^{v'J'} \rho_T(E_{vJ}^{v'J'}) \right] N_{v'J'} \right.$$
$$\left. - B_{v'J'}^{vJ} \rho_T(E_{v'J'}^{vJ}) N_{vJ} \right\} + \sum_{(v'J')<(vJ)} \left\{ B_{vJ}^{v'J'} \rho_T(E_{vJ}^{v'J'}) N_{v'J'} \right.$$
$$\left. - \left[A_{v'J'}^{vJ} + S_{v'J'}^{vJ} \rho_T(E_{v'J'}^{vJ}) \right] N_{vJ} \right\}, \quad (16)$$

where $\rho_T(h\nu)$ is the Planck distribution for radiation at temperature T at photon energy $h\nu = E_f^i = |E_f - E_i|$. Master equations of this type, possibly including further v- and J-dependent interactions of the stored ions, are used to model
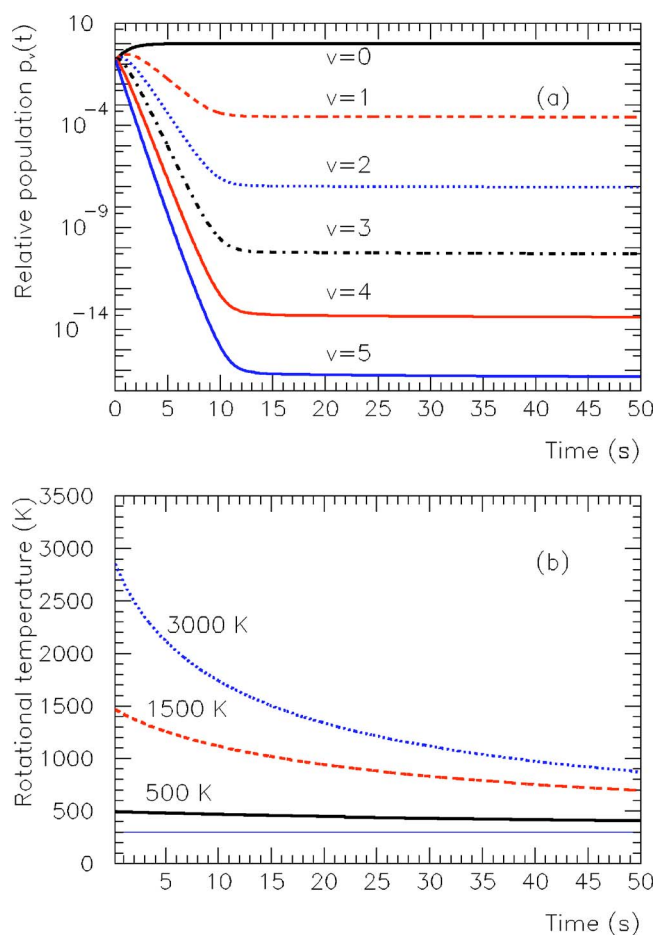
FIG. 5. (Color online) Radiative thermalization of rovibrational levels in the $X\,^2\Sigma_u^+$ electronic ground state of ^{3}He ^{4}He$^+$. (a) Vibrational thermalization among $v=0-5$. Initially, the six vibrational levels were populated equally, with a rotational temperature of 1500 K imposed on each level. (b) Rotational thermalization in the $v=0$ level for initial rotational temperatures of 500 K (solid), 1500 K (dashed), and 3000 K (dotted). The lowest line marks the 300 K equilibrium temperature.

the time evolution of level populations $p_{vJ}(t)$ in the stored ion beam, defined by $p_{vJ}(t)=N_{vJ}(t)/\Sigma_{v'J'}N_{v'J'}(t)$.

To illustrate the significance of radiative transitions on the evolution of the rovibrational population of the stored ion beam, and to predict the associated relaxation times, the coupled set of Eqs. (16) was solved for a Planck radiation field at 300 K for different initial populations (Fig. 5) using a fourth-order Runge-Kutta method for numerical integration.

Thermalization among the six lowest vibrational levels [Fig. 5(a)] occurs after $\sim$12 s; however, already at $\sim$5 s the populations of higher vibrational levels ($v\geq2$) are well below 10^{-4}, and the characteristic time scale for changes in the vibrational populations amounts to only $\sim$3 s. The rotational populations within the $v=0$ level [Fig. 5(b)] evolve over several tens of seconds, and thermalization is only reached after hundreds of seconds. If only radiative transitions were decisive for the evolution of the rovibrational population in the present measurements, higher vibrational states ($v\geq3$) would be essentially unpopulated after $\sim$3 s of storage and no contribution to the DR signal [Eqs. (5) and (14)] should

occur from these states despite a DR cross section four orders of magnitude larger than for the ground state ($v=0$).

3. Collisional effects on rovibrational populations

Collisions with both residual gas molecules and electrons are known to affect the rovibrational populations in stored beams of molecular ions [47–50]. The relevant elementary reactions between the stored He$_2^+$ ions and residual gas molecules in the present case would be collisions at MeV energies leaving the interacting He$_2^+$ intact, but changing its rovibrational excitation. In a photodissociation study of the stronger radiatively active molecular ion CH$^+$ [51] it was found that the ions do equilibrate with the 300-K radiation field, and effects of collisional induced rotational heating (expressed as an increase of the rotational temperature) were determined to be $\leq$10 K/s at similar residual gas densities as in the present experiment. In a study of HD$^+$ under similar conditions, evidence for a weak but measurable effect of vibrational excitation in the residual gas was reported [47,52].

The interaction with the electron beam can affect the rovibrational populations in two ways. First, different rate coefficients $\alpha_X^{vJ}(E_d)$ for electron-induced reactions X (in particular DR, possibly DE) can lead to different ion loss rate constants $k_X^{vJ}(E_d)$ [Eq. (12)] for the various rovibrational levels, leading to *preferential depletion* of levels with higher reaction rates. Indeed, in a recent study of the DR of D$_2$H$^+$ [48] this was considered as a mechanism likely to produce rotational populations in the ion beam with temperatures below the ambient blackbody radiation field. Second, (ro)vibrational transitions can be directly induced in electron collisions, as described by Eq. (3). In particular, vibrational excitation is likely to occur at collision energies in the eV range, as found for HD$^+$ [47,52]. Even if the interaction energy is tuned to small E_d in the central part of the electron cooler, higher electron collision energies occur over smaller portions in the toroid region (see Sec. II A) and can cause vibrational excitation.

On the other hand, at vanishing detuning energy E_d, where many of the present studies are performed, collisions in the central region of the electron cooler are characterized by very small interaction energies, as given by the electron temperature $kT_\perp=10$ meV. Under these conditions, the rate coefficients for superelastic collisions (SECs) [53] with vibrationally excited ions often exceed the DR rate coefficient, and the related vibrational de-excitation [cf. Eq. (3)] was indeed experimentally observed for H$_2^+$ [49,50] and D$_2^+$ [47].

Also in the present experiment on ^{3}He ^{4}He$^+$ the electron temperature $kT_\perp$ is well below the vibrational spacings, and of the order of the rotational spacings for low-lying J levels in the $v=0$ state. As purely rotational radiative transitions are relatively slow [see Figs. 4 and 5(b)], *rotationally* inelastic electron collisions may compete with them. With a rotational constant of $B_e=8.4$ cm$^{-1}\approx1$ meV [24] for ^{3}He ^{4}He$^+$, both excitation and de-excitation of rotational levels can be caused by electron collisions. The rates of rotationally inelastic low-energy electron-ion collisions have been considered theoretically for several molecular systems (see, for instance,

Refs. [54–56] and references therein), however, to the best of our knowledge no calculations exist for ^{3}He ^{4}He$^+$. The typical cross sections for these reactions are in the range of $10^{-14} - 10^{-12}$ cm^2 near their thresholds, and their effect on the present measurement can indeed be significant.

Collisional effects on the rovibrational populations in the stored ion beam will be further discussed below in Sec. VII B 2, considering both residual gas and electron collisions. The radiative rates of Eq. (16) will be complemented by approximate rate constants for inelastic collisions in order to obtain a rough model description of the rovibrational evolution under such effects. It should be emphasized that the evolution of the populations cannot generally be slowed down, but only accelerated by the occurrence of additional processes. Hence the *maximum* time scales over which the vibrational and rotational level populations evolve will still be given by the radiative time scales determined above.

III. COULOMB EXPLOSION DIAGNOSTICS

The relative vibrational level populations of the stored ^{3}He ^{4}He$^+$ ions were monitored with Coulomb explosion imaging (CEI) of ions slowly extracted from the beam during storage. Details about the CEI method and the setup at the TSR with the slow ion extraction can be found in Refs. [35,57,58]. Briefly, the extracted ions with kinetic energy $E_i = (M/2)v_i^2 = 7.28$ MeV were collimated by two 1-mm apertures 3 m apart, and then sent through a 80-Å-thick diamondlike carbon foil. The kinetic energy $\widetilde{E}_k$ released following the Coulomb explosion of individual molecular ions was determined downstream from the foil with a three-dimensional imaging technique [35].

For an ensemble of ions in a given vibrational state v, the distribution of kinetic energy releases after foil induced Coulomb explosion has a characteristic form $P_v(\widetilde{E}_k)$ [36] that reflects the distribution of nuclear positions and momenta in this state as well as the fragment scattering in the foil [59,60]. For an ensemble of ions in several vibrational states, the normalized kinetic-energy distribution after Coulomb explosion

$$P(\widetilde{E}_k, t) = \sum_v p_v(t) P_v(\widetilde{E}_k) \qquad (17)$$

is a superposition of the normalized distributions for the individual vibrational states, where the coefficients $p_v(t)$ represent the relative populations of the vibrational states v in the beam, and $\Sigma_v p_v(t) = 1$. The distributions $P_v(\widetilde{E}_k)$ were obtained by Monte Carlo simulations in close analogy to the procedure described in Ref. [36], combining a quantum-mechanical description of the Coulomb explosion process with a semiclassical ion propagation through the foil [59–61]. The accurate modeling of the distributions $P_v(\widetilde{E}_k)$ allows the relative distribution of vibrational states in the beam to be determined by fitting Eq. (17) to the experimental distribution with the relative populations $p_v(t)$ as free parameters.

Figure 6 displays normalized kinetic-energy distributions $P(\widetilde{E}_k, t)$ as measured with the CEI technique for three time
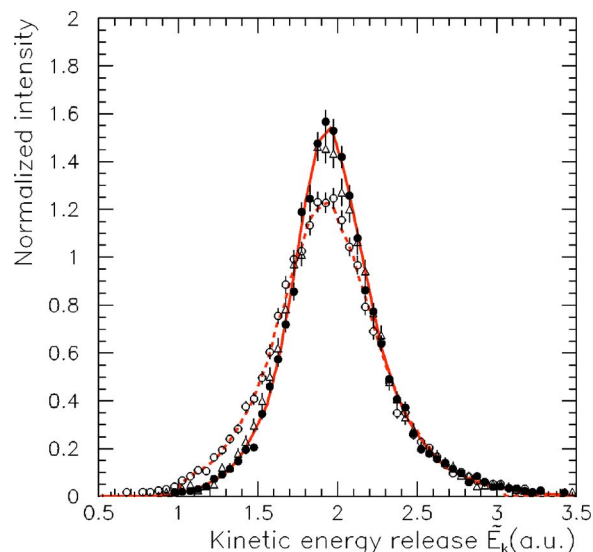

FIG. 6. (Color online) Normalized distributions of the kinetic-energy releases $(\widetilde{E}_k)$ after foil induced Coulomb explosion of ^{3}He ^{4}He$^+$ ions extracted from the stored beam when no electron cooling was applied. Distributions are shown for times after injection of 0–1 s (open circles), 2–3 s (triangles), and $\geqslant 3$ s (filled circles). The solid line show the simulated distribution for the ground state, and the dashed line shows the result of a least-squares fit with Eq. (17) to the distribution obtained at 0–1 s. Ion energy $E_i = 7.28$ Mev.

intervals after ion injection into the TSR when no electron cooling was applied. The kinetic-energy distribution is seen to become narrower with time, and the distribution seems to converge after 3 s, i.e., no change of the distribution could be observed when comparing distributions at different time intervals for $\geqslant 3$ s after injection. When no electron cooling is applied the rovibrational population of the ion beam is determined by radiative thermalization in competition with excitation through ion collisions with the residual gas (see Sec. II C 3). The relaxed kinetic-energy distribution $(t \geqslant 3$ s) without electron cooling compares very well with the Monte Carlo simulation for $P_{v=0}(\widetilde{E}_k)$. Performing a least-squares fit to the same distribution, using the superposition of simulated functions $P_v(\widetilde{E}_k)$ according to Eq. (17), yields $p_{v=0}(t \geqslant 3$ s$)$ $= (98.9 \pm 1.3)$ %. For the kinetic-energy distribution in an early phase of the vibrational relaxation $(t = 0$–1 s) the level populations are found from a similar fit to be (56 ± 3) % in $v=0, (13 \pm 4)$ % in $v=1, (16 \pm 5)$ % in $v=2$, and 15% distributed over the levels with $v \geqslant 3$. The evolution of the vibrational population was also measured while continuously applying electron cooling at all storage times, in parallel with the slow extraction. In this case, a least-squares fit to the converged distribution, using Eq. (17), yielded $p_{v=0}$ $= (91 \pm 14)$ %.

The CEI measurements demonstrate that the ion beam is dominated by the vibrational ground state $v=0$ after 3 s both with and without the presence of the electron beam during storage. This is consistent with the time scale of radiative thermalization, however nonthermal distributions with a few percent of the ions in higher vibrational states are also consistent with the data.

IV. ELECTRON-INDUCED REACTIONS

A. DR and DE rate measurements

Details of the experimental procedure for measuring rates of fragments from DE and DR reactions at the TSR have been described previously [32,33]. In the present measurement, the rates of neutral fragment events with total masses of 3, 4, and 7 amu were observed with the surface barrier detector (Sec. II A) as a function of the electron detuning energy E_d and the time t after the injection, yielding the quantities $R_{(7)}(E_d;t), R_{(3)}(E_d;t)$, and $R_{(4)}(E_d;t)$, respectively. The electron detuning energy could be cycled between the cooling energy $(E_d=E_d^c=0)$, a variable "measurement" energy E_d^m, and a "reference" energy E_d^r. After choosing E_d^r appropriately as described below, the full-mass count rate at the reference energy, $R_{(7)}(E_d^r;t)$, served for normalization with respect to the stored ^{3}He ^{4}He$^+$ ion current.

The energy dependences of the count rates R were usually obtained by cycling ("wobbling") between the three given levels of E_d at a dwell time of 50 ms on each of the levels. Following an injection of ions into the ring, E_d was first kept constant at $E_d^c=0$ for 5 s to allow for phase-space cooling and vibrational relaxation of the stored ion beam whereafter the electron energies E_d were wobbled as described. The value E_d^m was varied from one injection to the next. Energy- and time-dependent rates $R_{(7)}(E_d^m;t), R_{(3)}(E_d^m;t)$, and $R_{(4)}(E_d^m;t)$ were obtained from the detector counts accumulated over numerous injections, performing several scans of E_d^m over the desired range, where the counts for individual values of E_d^m and for individual bins of the ion storage time (i.e., the time after the injection into the storage ring) were added. With normalization and background subtraction as described below, rate coefficients $\tilde{\alpha}_{DR}(E_d;t)$ and $\tilde{\alpha}_{DE}(E_d;t)$ for the electron induced reactions were obtained. Time variations in these rate coefficients can arise from variations of the ^{3}He ^{4}He$^+$ level populations $p_{vJ}(t)$ in the stored beam [see Eq. (5)].

Apart from the wobble scheme, also much longer dwell times for E_d, ranging up to many seconds, were used in order to study the temporal behavior of the absolute and the normalized count rates, aiming at the determination of absolute rate coefficients and at the study of the level populations $p_{vJ}(t)$ of the stored ions. Measurements with both types of timing schemes will be discussed in the following.

1. Relative, energy-dependent count rates

Typical raw data for the DR and the DE channel, averaged over time intervals of 5–10 and 35–68 s and representing the relative rates $R_{(7)}(E_d^m;t)/R_{(7)}(E_d^r;t)$ and $R_{(3)}(E_d^m;t)/R_{(7)}(E_d^r;t)$, respectively, are shown in Fig. 7. In these data, as in the remainder of this paper, the reference energy was chosen as that of the prominent peak in the DR signal $R_{(7)}$, setting $E_d^r=7.3$ eV. The relative DR rate coefficient shown in Fig. 7(a) shows a considerable storage time dependence at $E_d \lesssim 0.1$ eV, while the high-energy structure does not vary significantly with the storage time. The absolute DR rate coefficient at E_d^r and the rate variations with the storage time will be considered further in the following. The DE rate in
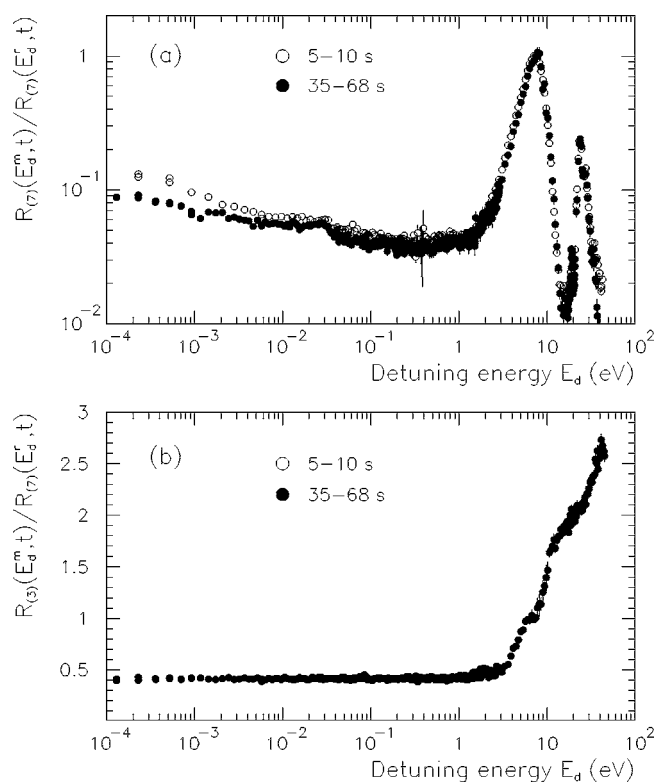

FIG. 7. Measured rates (raw data) of (a) DR and (b) DE events with normalization to the rate of DR events at the reference detuning energy ($E_d^r=7.3$ eV). Ion energy $E_i=7.28$ MeV; electron density $n_e=5.5\times10^6$ cm^{-3}.

Fig. 7(b) shows a threshold at $\sim$2.5 eV, corresponding to the dissociation energy of He$_2^+$. The nonzero rate $R_{(3)}$ below the threshold arises partly from DE events in the residual gas and partly from the toroid contribution discussed in Sec. II B.

2. Beam lifetime, reaction rate constants, and absolute rate coefficients

A series of measurements with long dwell times on different levels of E_d was performed in order to study the influence of electron and rest-gas induced reactions on the ion-beam lifetime, to clarify the relative significance of the various reaction rates considered in Sec. II C 1, and to obtain first information about the effects of time-varying internal excitations, as represented by $p_{vJ}(t)$. Moreover, these measurements yield an absolute calibration of our rate coefficients.

Figure 8 shows the time evolution of the absolute rates $R_{(7)}$ and $R_{(3)}$ for a situation where the electron beam was continuously on at $E_d=0$ for 10 s, whereafter it was switched off. The transient behavior observed in $R_{(3)}$ at <5 s can be attributed to changes in the ion-beam orbit and hence its pointing towards the detector during the initial electron cooling of the ion beam.

The full-mass rate $R_{(7)}$ shows a clearly nonexponential decrease up to the time when the electron beam is turned off, when it drops sharply, by more than two orders of magni-
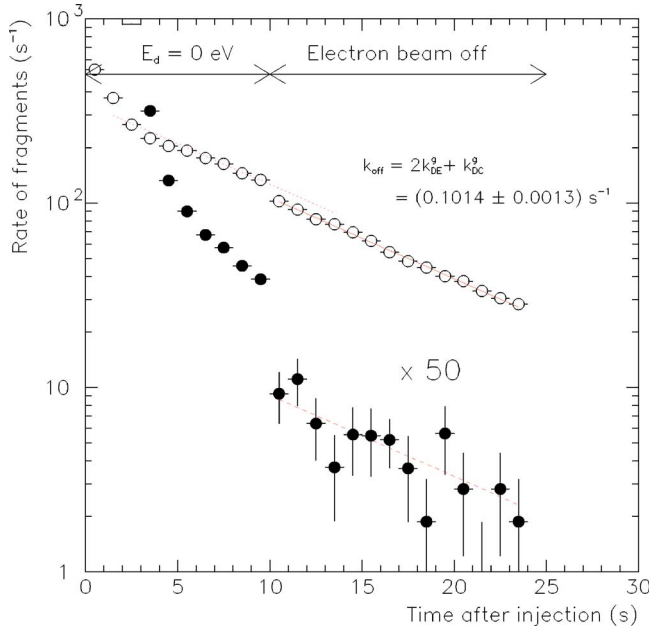
FIG. 8. (Color online) Measured fragment rates $R_{(7)}$ (filled circles) and $R_{(3)}$ (open circles) averaged over 76 injections when the electron beam is switched off after 10 s of storage. For times >10 s the values $R_{(7)}$ (solid circles) have been multiplied by a factor of 50. The solid line shows a single exponential fit to the rate $R_{(3)}$ at 10–23 s with the electron beam off, while the dashed lines compares the slope of the fitted curve to the rate $R_{(3)}$ at earlier times and to the rate $R_{(7)}$. Ion energy $E_i = 7.28$ MeV; electron density $n_e = 5.5 \times 10^6$ cm^{-3}.

tude. We conclude that this rate is dominated by DR and that the related rate constant $\widetilde{k}_{DR}(0; t)$ shows a significant time dependence, representing that of $p_{vJ}(t)$, which will be further investigated below. On the other hand, at times later than 5 s the decrease of $R_{(3)}$ is well described by a single exponential, both with and without the electrons. The jump in $R_{(3)}$ at the time when the electron beam is switched off indicates the presence of an electron-induced DE rate even at $E_d = 0$, representing the toroid contribution discussed above; this rate is represented by the term $\widetilde{k}_{DE}(0; t)$ in Eq. (15). From the observed step in $R_{(3)}$ at $t = 10$ s, we find the size of this contribution relative to the rest-gas rate constant as

$$c_1 = \widetilde{k}_{DE}(0)/f_g k_{DE}^g = 0.18(2). \qquad (18)$$

No significant time dependence of $\widetilde{k}_{DE}(0)$ is observed, as $R_{(3)}$ decreases as a single exponential even with the electrons present.

The time dependence of $R_{(3)}$ at $t > 10$ s reveals the beam loss due to rest-gas induced processes, described by $\dot{N}_i(t) = -k_{off} N_i(t)$ with $k_{off} = 2k_{DE}^g + k_{DC}^g$ [cf. Eq. (13)]. Dissociative charge exchange (DC) in the rest gas is much less likely than DE, as revealed by the ratio $R_{(7)}/R_{(3)}$ without electron beam, which yields with the help of Eqs. (14) and (15)
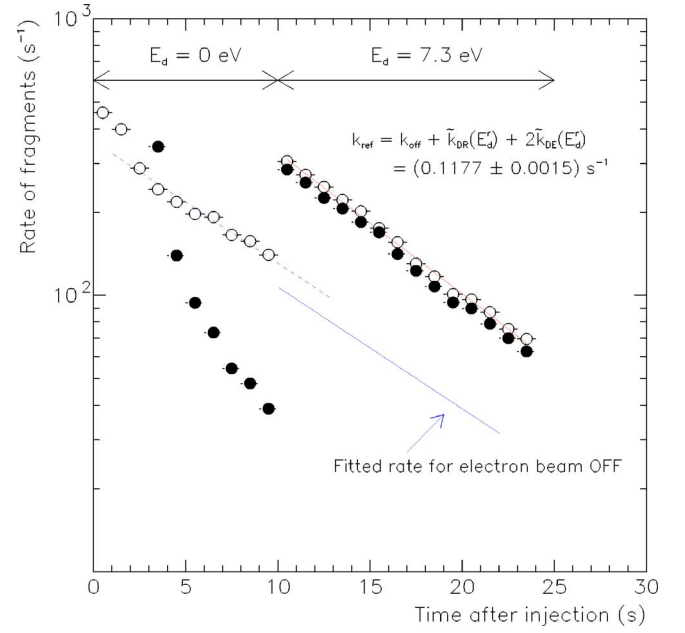

FIG. 9. (Color online) Measured rates $R_{(7)}$ (filled circles) and $R_{(3)}$ (open circles) average over 33 injections as a function of time t after injection where the detuning energy E_d was changed from 0 to 7.3 eV at $t = 10$ s. The upper solid line shows a single exponential fit to the rate $R_{(3)}$ at 10–23 s, while the lower dashed and soild lines are repeated from Fig. 8.

$$c_2 = k_{DC}^g/k_{DE}^g = 1.6(2) \times 10^{-3}. \qquad (19)$$

From the experimental result $k_{off} = 0.1014(13)$s^{-1} one can then deduce

$$k_{DE}^g = k_{off}/(2 + c_2) = 0.0506(7)\text{s}^{-1} \qquad (20)$$

together with $k_{DC}^g = 8(1) \times 10^{-5}$ s^{-1}.

The measurement of Fig. 8 was repeated immediately, under the same vacuum conditions, now changing the electron energy E_d from 0 to $E_d^r = 7.3$ eV at $t = 10$ s (see Fig. 9). The full-mass rate $R_{(7)}$, showing the same nonexponential behavior as before for $E_d = 0$, increases strongly as E_d is stepped up to E_d^r and turns over to a single-exponential decay. The decay rate of $R_{(7)}$ for $t > 10$ s is the same as that of $R_{(3)}$ within the experimental accuracy and amounts to $k_{ref} = 0.1177(15)$s^{-1}.

The single-exponential decays of $R_{(7)}$ and $R_{(3)}$ at E_d^r indicate that $\widetilde{k}_{DR}(E_d^r)$ and $\widetilde{k}_{DE}(E_d^r)$ are time independent, i.e., they reveal no influence due to possible time variations of the level populations $p_{vJ}(t)$. Using Eqs. (14), (15), (18), and (19) to express the measured ratio $c_3 = R_{(7)}(E_d^r)/R_{(3)}(0) = 2.56(7)$ from Fig. 9, one finds

$$\frac{\widetilde{k}_{DR}(E_d^r)}{f_g k_{DE}^g} = c_3(1 + c_1) - c_2. \qquad (21)$$

Using this result and expressing in a similar way the measured ratio $c_4 = R_{(3)}(E_d^r)/R_{(7)}(E_d^r) = 1.02(1)$ from Fig. 9, one finds that the ratio of the DE and DR rate constants at the reference energy can be expressed as

$$\rho_{DE} = \frac{\tilde{k}_{DE}(E_d^r)}{\tilde{k}_{DR}(E_d^r)} = \frac{c_3 c_4 (1 + c_1) - 1}{c_3 (1 + c_1) - c_2}. \qquad (22)$$

Evaluation of this expression yields $\rho_{DE} = 0.690(14)$. The decays of both $R_{(7)}$ and $R_{(3)}$ finally reflect the decrease of the ion number according to $\dot{N}_i(t) = -k_{ref} N_i(t)$ with $k_{ref} = k_{off} + \tilde{k}_{DR}(E_d^r) + 2\tilde{k}_{DE}(E_d^r)$ [cf. Eq. (13)]. With the help of Eq. (22) it is then possible to obtain the absolute DR rate coefficient at E_d^r as

$$\tilde{\alpha}_{DR}^{c+tor}(E_d^r) = \frac{\tilde{k}_{DR}(E_d^r)}{\eta n_e} = \frac{k_{ref} - k_{off}}{\eta n_e [1 + 2\rho_{DE}]}. \qquad (23)$$

Here, $\tilde{\alpha}_{DR}^{c+tor}(E_d^r)$ is used to denote the sum of the contributions from the central and the toroid sections, occurring in Eq. (7); a toroid correction (which is small at $E_d = E_d^r$) will be applied in Sec. IV A 3. With the known values of $n_e(E_d^r) = 7.9 \times 10^6$ cm^{-3} and $\eta = 0.027$ we obtain $\tilde{\alpha}_{DR}^{c+tor}(E_d^r) = 3.2(4) \times 10^{-8}$ cm^3 s^{-1} in the particular example described above.

One also obtains, with the known DR rate constant $\tilde{k}_{DR}(E_d^r)$ and the absolute rate constant k_{DE}^g for DE on rest-gas from Eq. (20), the efficiency f_g for detecting rest-gas events, which results in 0.044(7) and hence in an "observed" effective ion-beam length of ~2.4 m, in reasonable agreement with the geometrical conditions of the experiment.

The above described procedure to obtain an absolute DR rate coefficient relies on the assumption that the presence of the electron beam does not affect the vacuum significantly in the region of the electron cooler, i.e., that the values of k_{DC}^g and k_{DE}^g are unaffected by the presence of the electron beam. To investigate the validity of this assumption we made measurements similar to the ones in Figs. 8 and 9, but now changing the detuning energy from zero to 0.5 eV at 10 s. As can be derived from Fig. 7 the electron-induced reactions at 0.5 eV are relatively small, and the decay of the stored ion-beam is determined mainly by DE in the residual gas (k_{DE}^g). With $E_d = 0.5$ eV, an ion-beam decay rate of $k_{0.5\ eV} = 0.0994(15)$s^{-1} was obtained, in consistency with the value k_{off} obtained without the electron beam. Hence the electron beam does not affect the beam decay significantly through an increase of vacuum pressure, and the assumptions underlying the above derivation are indeed justified.

Repeated measurements of the rate coefficient at E_d^r as described above yielded values that scattered around those obtained in the example discussed. As the final normalization of the measured rate coefficient we use the weighted average of the different measurements and give their standard deviation as the uncertainty, yielding $\tilde{\alpha}_{DR}^{c+tor}(E_d^r) = 2.8(4) \times 10^{-8}$ cm^3 s^{-1}.

Altogether, the time dependences of the absolute count rates show a markedly nonexponential decay for the full-mass events near zero energy, indicating an influence of internal relaxation of the stored ions on their DR rate. For high-energy DR, no such influence is observed, and a com-
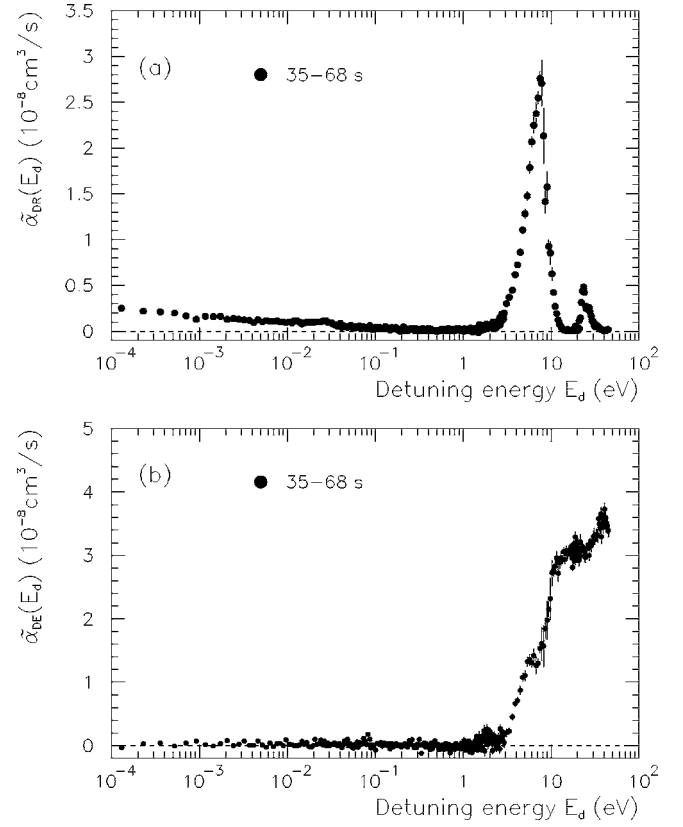

FIG. 10. Rate coefficients as a function of the detuning energy E_d measured in a time interval of 35–68 s after ion injection. (a) Toroid corrected DR rate coefficient over the full energy range studied. The dashed line marks the zero on the vertical scale. (b) Toroid corrected DE rate coefficient. Ion energy $E_i = 7.28$ MeV; electron density $n_e = 5.5 \times 10^6$ cm^{-3}.

parison of the decay rates with and without electrons can be used to obtain the DR rate coefficient on the peak at 7.3 eV, providing a useful absolute normalization.

3. Energy dependent rate coefficients

From the relative rate shown in Fig. 7, the absolute DR rate coefficients can now be determined using the relation

$$\tilde{\alpha}_{DR}^{c+tor}(E_d; t) = \tilde{\alpha}_{DR}^{c+tor}(E_d^r) \frac{R_{(7)}(E_d; t)}{R_{(7)}(E_d^r; t)} \frac{n_e(E_d^r)}{n_e(E_d)}. \qquad (24)$$

Here, the very small background from DC in the residual gas contained in the rate $R_{(7)}$ can be safely neglected. Since the DR rate coefficient for energies outside the scanned energy region can be assumed to vanish, the standard iterative procedure [34,43] can be used to obtain the toroid-corrected DR rate $\tilde{\alpha}_{DR}(E_d; t)$, shown for the relaxed beam ($t = 35$–68 s) in Fig. 10(a). The toroid contribution to the low-energy part of the DR rate coefficient measurement is illustrated by Fig. 11. Its size relative to the corrected rate coefficient at $E_d = 0$ is found to be $\tilde{\alpha}_{DR}^{tor}(0) / \tilde{\alpha}_{DR}(0) = 0.34(6)$.
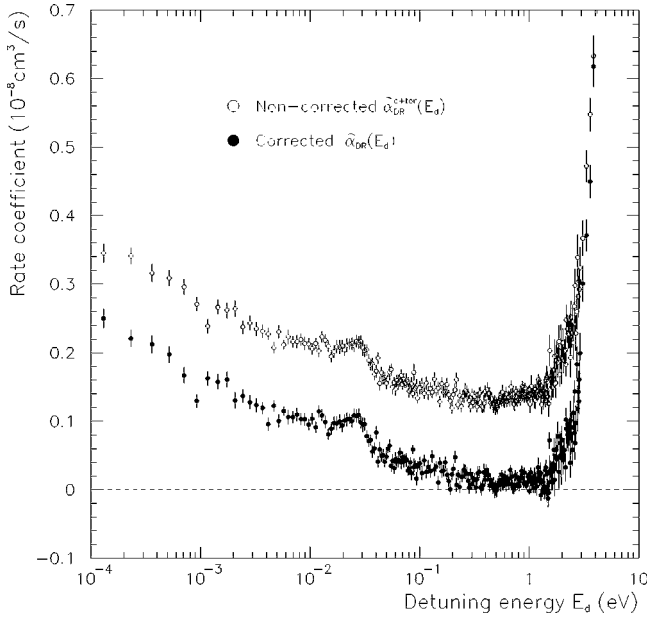
For DE, the rate coefficient is obtained as

FIG. 11. Effect of the toroid correction on the DR rate coefficient displayed in Fig. 10(a) in the low-energy region. The upper curve (open circles) shows the directly obtained rate coefficient $\tilde{\alpha}_{DR}^{c+tor}(E_d)$ while the lower curve (filled circles) shows the rate coefficient $\tilde{\alpha}_{DR}(E_d)$ after toroid correction.

$$\tilde{\alpha}_{DE}^{c+tor}(E_d;t) = \tilde{\alpha}_{DR}^{c+tor}(E_d^r)\frac{n_e(E_d^r)}{n_e(E_d)}$$

$$\times \frac{R_{(3)}(E_d;t) - R_{(3)}(0;t)(1-\varepsilon_{tor})}{R_{(7)}(E_d^r;t)}, \quad (25)$$

where the background contribution to DE from the residual gas only is subtracted, i.e., $\varepsilon_{tor}=\tilde{k}_{DE}(0)/[f_g k_{DE}^g + \tilde{k}_{DE}(0)]$. During the experimental runs, small temporal variations of the vacuum conditions produce changes in the residual gas rate constant k_{DE}^g. For the particular residual gas pressure present when the data used to derive c_1 in Eq. (18) was taken, we obtain $\varepsilon'_{tor}=c_1/(1+c_1)=0.15(2)$. Since $\tilde{k}_{DE}(0)$ is vacuum independent, the value of ε_{tor} can directly be obtained as $\varepsilon_{tor}=\varepsilon'_{tor}[R'_{(3)}(0;t)/R'_{(7)}(E_d^r;t)]/[R_{(3)}(0;t)/R_{(7)}(E_d^r;t)]$, where $R'_{(3)}(0;t)$ and $R'_{(7)}(E_d^r;t)$ are the observed rates of Figs. 8 and 9.

The toroid correction of the DE rate is expected to be reliable up to $E_d \sim 25$ eV. Above this value an assumption about the further energy dependence of the DE rate coefficient from 40 eV up to ~55 eV is required. We assume as a resonable approximation that the rate coefficient stays constant in this range at the value measured at 40 eV. The DE rate coefficient corrected under this assumption, $\tilde{\alpha}_{DE}(E_d;t)$, is shown in Fig. 10(b) for $t=35$–68 s. It should be noted that the toroid correction brings the DE rate at low energy to zero. Indeed, this verifies in a sensitive manner that the identification of the step in the rate $R_{(3)}$ of Fig. 8 is correct.

B. DR fragment imaging

The event-triggered fragment imaging detection system mentioned in Sec. II A yields the transverse positions of cor-

related pairs of neutral ^{3}He and ^{4}He fragments released in single DR reactions. Distributions of the transverse distance between such correlated product atoms reveal the kinetic-energy release (KER) of the DR events. The KER in turn can provide a signature of the internal excitation present in the reacting ^{3}He ^{4}He$^+$ ions.

Fragment imaging measurements were performed only at $E_d=0$ and served particularly to clarify the effect of internal excitations on the low-energy DR rate coefficient $\tilde{\alpha}_{DR}(0;t)$, found to display a significant time depencence in the measurements of Sec. IV A. Here, we will first consider the experimental framework, analysis, and basic observation related to fragment imaging of ^{3}He ^{4}He$^+$ DR reactions. Similar to the rate coefficient $\tilde{\alpha}_{DR}(0;t)$, also the fragment imaging distributions show a time dependence, whose basic phenomenology will be presented in this section. In a next step (Sec. V) we will describe series of dedicated experiments where both rate coefficient and fragment imaging measurements are used as tools for understanding the nature and the origin of the rovibrational excitation in the stored ^{3}He ^{4}He$^+$ ion beam.

1. Fragment imaging experimental conditions

Following a reaction of ^{3}He ^{4}He$^+$ with the residual gas or with electrons, either one or two neutral fragments arrive at the detector, which for unit detection efficiency and a perfect single-event trigger scheme would yield corresponding one-body (single) or two-body (double) events. The *observed* numbers $\tilde{N}_s$ and $\tilde{N}_d$ are reduced with respect to the true event numbers N_s and N_d due to the finite detection efficiency of the MCP detector.

As the fragments are identified by the light spots they generate on the detector screen, a two-body event with a small transverse distance can in addition be falsely identified as a one-body event, in case the light spots overlap. This results in a limited detection for DR events with small KER.

The measured fragment rates were kept below 10^3 s^{-1} in all runs. The ratio of detected double to single events was found to vary between 0.15 and 0.03. With an effective coincidence time window of the event trigger scheme of ~10 μs, the false coincidence contribution is expected to stay below 1%. Accordingly, the ratio of (false) triple events to the doubles was found to be well below 1%. We hence consider that false coincidences can be neglected.

Assuming that the fragment masses are identified, the co-ordinates of the center of mass (c.m.) can be determined for correlated two-body events. The c.m. coordinates represent the transverse motion of the interacting ^{3}He ^{4}He$^+$ ions, propagated on a straight line from the location of the DR event to the detector. Although the present fragment imaging system does not allow the masses to be identified, the c.m. coordinates can be reconstructed for, on the average, 50% of all events by assigning the masses of 3 and 4 amu, respectively, arbitrarily to the individual fragments in each observed correlated pair. The observed pattern of c.m. positions in the transverse plane, shown in Fig. 12(a) for an electron energy $E_d=0$, reveals different contributions to the low-energy DR rate. One contribution has circular symmetry and is located near the nominal beam axis of the straight storage
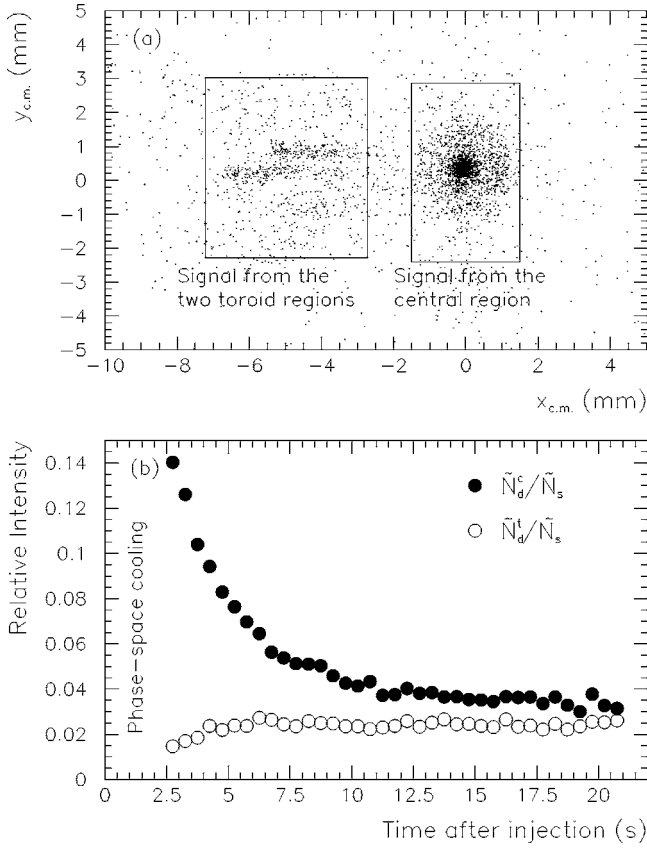
FIG. 12. DR (two-body) events recorded with the fragment imaging technique. (a) Two-dimensional distribution of events according to their c.m. positions $x_{c.m.}, y_{c.m.}$. (b) Time evolution of the signal from the central part (filled circles) and the toroid part (open circles) of the electron cooler with normalization to the apparent one-body events ($\tilde{N}_s$).

ring section to which the detector is aligned (zero point of the x-y plane). Two additional, horizontally elongated structures appear at $-7 < x_{c.m.} < -3$ mm and $-0.5 < y_{c.m.} < 1.5$ mm. While all contributions must arise from electron interaction (see Sec. IV A 2), the circular part can be assigned to the straight (central) overlap section of the electron cooler, while the two elongated structures clearly originate from the two toroid regions, where the electron beam is guided in and out of the ion orbit. In fact, the ion beam is horizontally deflected by the magnetic field of the toroids [43], whose bending plane is oriented vertically. As expected, the main contribution from the toroids does not arise close to the beam merging region, where the electron interaction energy is still close to $E_d=0$, but further up or down the bends, where the interaction energy reaches values close to 7 eV, i.e., around the peak in the DR rate coefficient [see Fig. 7(a)]; here, the ion beam is already bent substantially from its aligned direction in the overlap region. Note that in Fig. 12(a) the narrow circular peak near the zero point of the x-y plane is surrounded by a more diffuse distribution of events which represents those events for which the arbitary assignment of the individual fragment masses was incorrect. Yet, by suitable cuts on the c.m. positions as indicated in Fig. 12(a), the fragment imaging data for $E_d=0$ can be decom-

posed into separate contributions from the linear overlap region of the electron cooler and from the toroid regions.

The described assignment of the c.m. position ranges is further supported by the time depencence of the rates $\tilde{N}_d^c$ and $\tilde{N}_d^t$ for the central and the toroid region, respectively. These rates are shown with a normalization to the observed rate of single events, $\tilde{N}_s$, in Fig. 12(b). The relative rate $\tilde{N}_d^c/\tilde{N}_s$ shows a significant time variation over up to 20 s, similar to the variation of the DR rate constant at $E_d=0$ discussed in Sec. IV A 2. In contrast, $\tilde{N}_d^t/\tilde{N}_s$ settles to a constant value much faster, in consistency with the observation of a fixed DR rate constant for $E_d=7.3$ eV in Sec. IV A 2.

2. Fragment imaging distributions

The analytical description of transverse (projected) interparticle distance distributions for DR fragment imaging of diatomic molecular ions has been discussed in detail earlier [36]. At vanishing electron collision energy ($E_d=0$; thermal electron energy neglected) the kinetic energy release E_k for well defined initial state v, J and final atomic states n, n' can be written as

$$E_k^{vJnn'} = E_{vJ} - E_{nn'}, \qquad (26)$$

where E_{vJ} denotes the initial molecular energy level and $E_{nn'}$ the asymptotic energy level of the atomic fragments. Each contribution with a given kinetic-energy release is associated with a characteristic distribution $P_{vJnn'}(D)$ [36] of projected distances, displaying an end point at the maximal transverse distance

$$D_{max} = s_{max} \frac{M(^3\text{He}) + M(^4\text{He})}{\sqrt{M(^3\text{He})M(^4\text{He})}} \sqrt{\frac{E_k^{vJnn'}}{E_i}}, \qquad (27)$$

where s_{max} denotes the maximum possible distance from a DR interaction point to the detector (in the present setup $s_{max}=7.17$ m, corresponding to the far end of the central electron interaction region as seen from the fragment imaging detector). With given molecular level populations $p_{vJ}(t)$ and with the DR rate coefficients $\alpha_{DR}^{vJnn'}(0)$ for specific initial and final states, the total spectrum of measured projected distances can be written as the superposition

$$P(D,t) = K(t) \sum_{vJnn'} p_{vJ}(t) \alpha_{DR}^{vJnn'}(0) P_{vJnn'}(D), \qquad (28)$$

where $K(t)$ is a normalization factor. As contributions from various rotational levels cannot be resolved, the distinct features in the projected distance distribution are associated with individual vibrational levels and individual atomic quantum numbers n, n'. Using J-averaged DR rate coefficients $\tilde{\alpha}_{DR}^{vnn'}(0)$ and distance distributions $\tilde{P}_{vnn'}^{(T_{rot})}(D)$, taking into account the rotational energy and thermal rotational level populations for a suitable temperature T_{rot} [36], the superposition of Eq. (28) is then represented as

$$P(D,t) = K(t) \sum_{vnn'} p_v(t) \widetilde{\alpha}_{DR}^{vnn'}(0) \widetilde{P}_{vnn'}^{(T_{rot})}(D). \qquad (29)$$

The distributions of relative distances between fragments from DR reactions as obtained with the fragment imaging technique reveal information on the relative contributions to the overall DR rate from different reaction channels vnn', as characterized by $p_v(t)\widetilde{\alpha}_{DR}^{vnn'}(0)$. For assigned vibrational levels v, these data also yield the branching ratios to the possible atomic final states.

The DR fragment imaging measurements discussed below were performed at an ion energy of $E_i=3.36$ MeV using a detuning energy $E_d=0$ (where the electron density amounted to $n_e=5.5\times10^6$ cm^{-3}). Figure 13(a) shows as an example the analytical shape of the projected distance distribution for $v=0, J=0$ and for the final channel He$(1s^2)$+He$(1s2s^3 S)(E_k=2.41$ eV), together with the end points for other possible final states with $n=2$ and 3, as reached from the vibrational levels $v=0$–6. As seen in Fig. 1, the zero-energy DR of ^{3}He ^{4}He$^+$ ions in the vibrational states $v \geqslant 3$ can also lead to the $n=3$ final atomic states, associated with much smaller kinetic-energy release. In the observed projected distance distributions, contributions with end points at small D therefore indicate the presence of vibrationally excited ions in levels $v \geqslant 3$, and can *only* arise from such levels.

The projected distance distributions observed with a stored ^{3}He ^{4}He$^+$ beam for different time intervals after the injection are shown in Figs. 13(b)–13(d). A prominent contribution at low distances D, clearly arising from vibrationally excited ions in $v \geqslant 3$, can be seen at all times, although its relative size decreases substantially during the first ~ 10 s of storage time. The peak at large distances becomes narrower at later storage times. Two regions showing different types of temporal behavior can be identified, with a border at $D \sim 7$ mm. Limited detection of fragment pairs, as discussed in Sec. IV B 1, occurs at $D < 2.5$ mm.

The fragment distributions of Fig. 13 include data only from the central part of the electron-ion interaction region, corresponding to the "central region" c.m. cut shown in Fig. 12(a). For the toroid regions, much different projected distance distributions are observed (not shown). They are characterized by much higher energy release, dominated by the dissociation dynamics on the high-energy peak of the DR rate coefficient between 5 and 9 eV.

It is interesting to note that the projected distance distribution from the toroid regions has only a minor contribution at small distances and therefore is only slighty affected by the limited detection of fragment pairs with small D. This opens up the opportunity of finding the fraction of events suppressed by limited detection at small D in the fragment distributions from the central part of the interaction region. Using the solid-state detector, offering unit detection efficiency, the size of the toroid contribution relative to the DR rate from the central region of the electron cooler was determined in Sec. IV A 3 to amount to $\widetilde{\alpha}_{DR}^{tor}(0)/\widetilde{\alpha}_{DR}(0)=0.34(6)$. On the other hand, Fig. 12(b) shows a ratio between the double-hit events from the toroid and the central region of $\widetilde{N}_d^t/\widetilde{N}_d^c=0.67(10)$ for $t > 15$ s. Assuming that the toroid contribution on the imaging detector, $\widetilde{N}_d^t$, is not influenced by
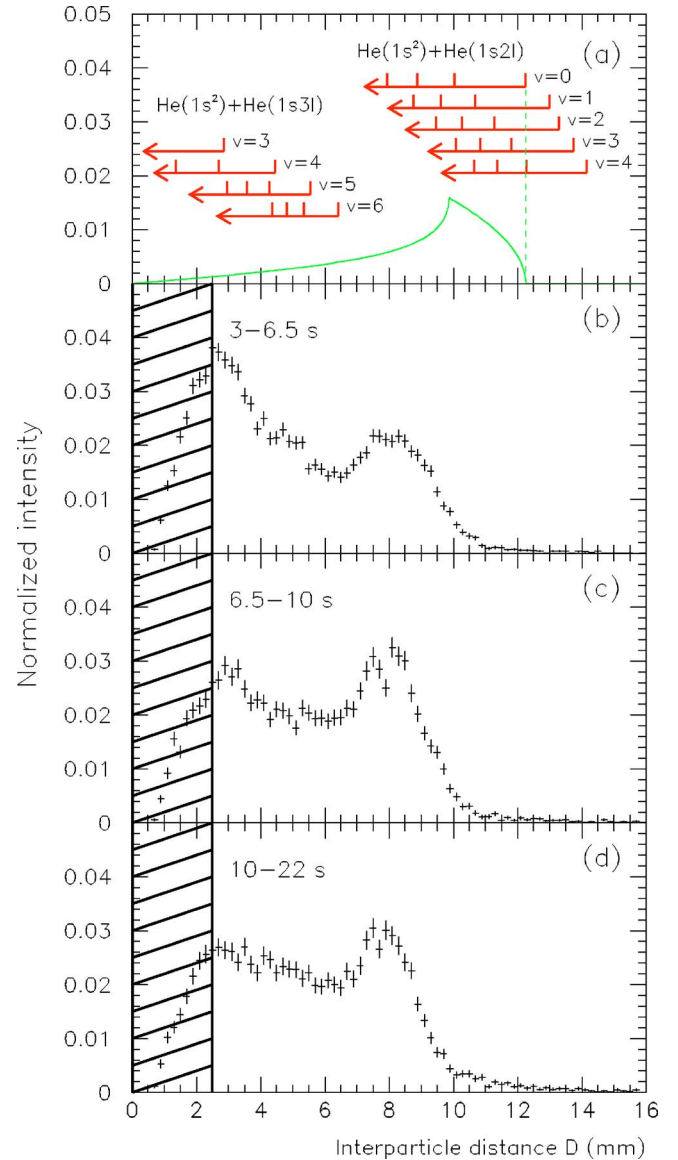

FIG. 13. (Color online) Distributions of projected interparticle distances (D) from DR (two-body) events in the central part of the electron cooler at zero detuning energy E_d. (a) Analytical form of the distribution for a special case (see text) and end points (marked by vertical ticks on arrows) for various possible initial-to-final-state channels. The lower frames show experimental results for time intervals of (b) 3–6.5 s (c) 6.5–10 s, and (d) 10–22 s. The hatched area at low distance marks the region of limited detection due to overlapping light spots on the phosphor screen. Ion energy $E_i=3.36$ MeV; electron density $n_e=5.5\times10^6$ cm^{-3}.

limited detection, while the central contribution is reduced through this effect by a factor of $1-\widetilde{f}_d$, the missing fraction $\widetilde{f}_d$ can be determined to

$$\widetilde{f}_d = 1 - \frac{\widetilde{\alpha}_{DR}^{tor}(0)/\widetilde{\alpha}_{DR}(0)}{\widetilde{N}_d^t/\widetilde{N}_d^c} = 0.49(11) \qquad (30)$$

for times larger than 15 s after injection. In Sec. VI B this number will be used to evaluate the absolute DR rate coefficient for the $v=0$ level.

V. ROVIBRATIONAL EXCITATION AND COOLING OF THE STORED ION BEAM

As illustrated in Sec. II C 2, radiative thermalization with the blackbody radiation at 300 K would make the ion beam dominated by the vibrational ground state with $p_{v=0}$ >99.9% after 10 s of storage, leaving <0.1% in all higher vibrational states [see Fig. 5(a)]. However, the rotational radiative relaxation is expected to be much slower [Fig. 5(b)]. Moreover, a number of processes beyond radiative transitions were discussed in Sec. II C 3 that may modify the rovibrational populations. Hence internal excitations in the stored molecular ion beam deserve careful consideration.

The Coulomb explosion measurements described in Sec. III confirm the vibrational relaxation of the ions with a possible remaining excited-state population at the percent level for the case that no electrons are present. In the presence of electrons a similar vibrational relaxation is seen, but the observational uncertainties would allow the excited-state populations to exceed the 10% level. Based on these measurements and considering the expected large increase of the He_2^+ DR rate coefficient for increasing vibrational excitation, the excited-state populations in the stored ion beam can still be sufficiently large to cause significant contributions to the observed neutral fragment rates. Regarding rotations, the Coulomb explosion imaging method is unfortunately not suited to characterize the excited level populations.

In this section, a series of arguments and dedicated measurements is described which attempts to clarify in detail the influence of internal molecular excitations on the present data and to identify processes beyond blackbody-driven radiative interactions that determine the evolution of rovibrational populations in the stored ion beam. From the evidence obtained, it then becomes possible to extract quantitative, initial- and final-state specific information on the DR of ^{3}He ^{4}He$^+$ (Sec. VI). A further discussion using a model description of rovibrational excitation and de-excitation (Sec. VII B) will finally allow the cross sections of the underlying inelastic processes to be quantitatively characterized.

A. Time dependence of zero-energy DR rate

Figure 14 shows the ratio $R_{(7)}/R_{(3)}$ at $E_d=0$ for conditions where the electron beam was either continuously on or switched off for different segments of time after the end of the phase-space cooling. Following Eqs. (14) and (15) and noting the time independence of $\tilde{k}_{DE}(0)$ (Sec. IV A), this ratio is proportional to the rovibrationally averaged DR rate constant $\tilde{k}_{DR}(0;t)$ and hence probes the evolution of the rovibrational population in the ion beam if the DR rate coefficients of the rovibrational levels differ from each other [see Eq. (5)].

As seen in Fig. 14, when the electron beam is continuously on, $\tilde{k}_{DR}(0;t)$ decreases strongly until an apparently constant level is reached after about 30 s. The shape of the curve cannot be well described by a simple function such as a single exponential plus a constant or the sum of two exponentials. When the electron beam has been off for one of the
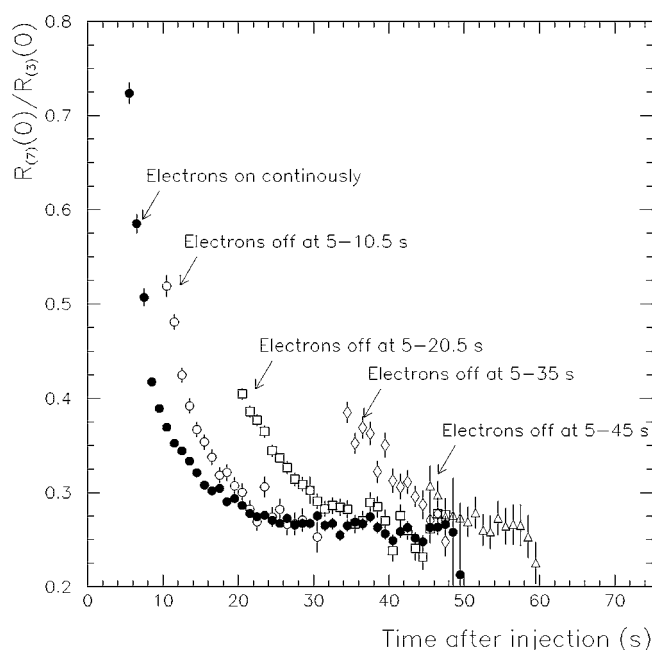

FIG. 14. Measured DR rate $R_{(7)}(0)$ normalized to $R_{(3)}(0)$ for situations where the electron beam was continuously on (filled circles), and switched off at 5–10.5 s (open circles), 5–20.5 s (open squares), 5–35 s (open diamonds), and 5–45 s (open triangles). Ion energy $E_i=7.28$ MeV; electron density $n_e=1.2\times10^7$ cm^{-3}.

various segments of time, a larger value of $R_{(7)}/R_{(3)}$ is observed when switching it back on as compared to the situation where the electron beam is continuously on. However, after switching the electron beam on again, $R_{(7)}/R_{(3)}$ decreases on a time scale of ~10 s to the level reached with the electron beam continuously on. The effect of the electron beam on the rovibrational population is further emphasized by the data shown in Fig. 15, which displays the value of $R_{(7)}/R_{(3)}$ for two different electron densities. A higher electron density leads to a faster approach to the asymptotic DR rate, while the final asymptotes are similar. The electron-beam-dependent behaviors illustrated in Figs. 14 and 15 clearly show that the DR reaction rate depends upon the rovibrational state and that the electron beam indeed influences the rovibrational population in the beam.

Moreover, as seen in Fig. 14, the value of $R_{(7)}/R_{(3)}$ *at the moment* when the electron beam is switched back on decreases with longer periods without electron cooling. This proves unambiguously that the rovibrational population in the ion beam evolves over tens of seconds even if only radiative transitions and residual gas collisions can occur. The electron beam was also switched off for a similar period as in Fig. 14 at later times after injection (35–50 s), i.e., after $R_{(7)}/R_{(3)}$ had already reached its asymptotic value. In this test (not shown in Fig. 14) no significant change of the ratio $R_{(7)}/R_{(3)}$ could be seen when switching the electron beam back on. Hence on a time scale of 15 s the asymptotic rovibrational population reached after continuous electron interaction is not altered under the combined influence of blackbody radiation and residual gas collisions.

Using the estimates on the rovibrational evolution given in Sec. II C 2 it is possible to understand more precisely the
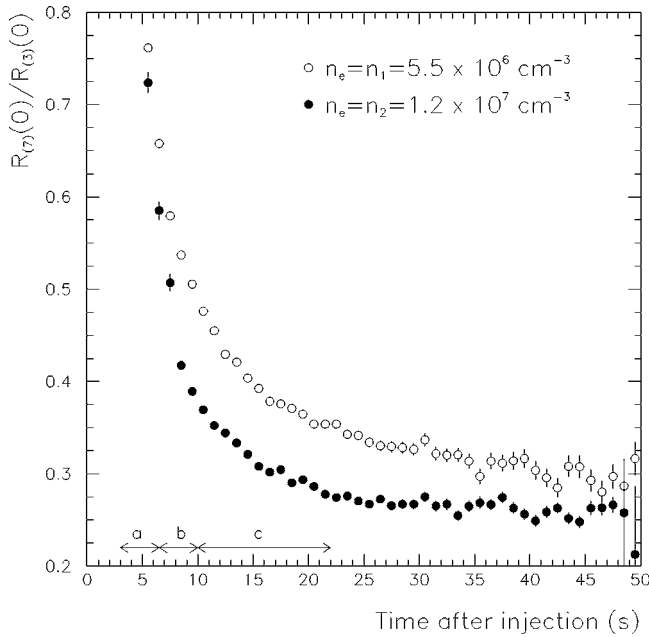
FIG. 15. Measured DR rates $R_{(7)}(0)$ normalized to $R_{(3)}(0)$ measured with the electron beam continuously on for electron densities of $n_e = n_1 = 5.5 \times 10^6$ cm^{-3} (open circles) and $n_e = n_2 = 1.2 \times 10^7$ cm^{-3} (filled circles). To compare the relative rate $R_{(7)} \times (0)/R_{(3)}(0)$ at the two different electron densities the data measured for n_1 have been scaled with the help of Eqs. (14), (15), and (18) by the factor $n_2(1+1/c_1)/(n_2+n_1/c_1)=1.77$. Ion energy $E_i = 7.28$ MeV. The time intervals marked a, b, and c are those for which fragment imaging spectra are presented in Fig. 13.

origin of the signal evolutions shown in Figs. 14 and 15. Radiative transitions drive the vibrational population of the stored ions to stabilize within a few seconds after injection, and the fast decay of the DR rate up to ~ 10 s could well represent the vibrational stabilization. That the vibrational stabilization is observed for longer times than seen with the CEI technique is expected since the DR measurements are much more sensitive to higher vibrational states, given the larger DR cross sections for these as compared to the vibrational ground state $v=0$ [10]. The final vibrational populations in the beam cannot be estimated based on the results in Figs. 14 and 15, but will be discussed in Sec. V B.

Based on its time scale, the following evolution of the DR signal over tens of seconds, i.e., beyond 10 s in Figs. 14 and 15, must originate from changes in the *rotational* populations. As a first consequence, this demonstrates that the DR cross section depends on the initial rotational state of the interacting ion. In Sec. II C 3 two possible effects of the electron beam on the rotational populations were discussed: preferential depletion of specific J levels by the DR reaction, or their electron-impact excitation and de-excitation [Eq. (3)].

Preferential depletion by the DR reaction would produce a significant effect on the beam decay, which was not observed in the measurements of Sec. IV A (see Fig. 8). Moreover, the electron induced rate variation seen in Fig. 14 when switching the electron beam back on occurs over a time scale of ~ 10 s. With the applied electron density of n_e

$=1.2 \times 10^7$ cm^{-3}, the rate coefficients involved in the underlying changes of the rotational level populations should have a size of ~ 10 s $(\eta n_e)^{-1} = 3 \times 10^{-7}$ cm^3/s. On the other hand, the observed absolute DR rate coefficient at $E_d = 0$ (including contributions from excited states with $v \geqslant 3$) amounts to only $\sim 3 \times 10^{-9}$ cm^3/s [see Fig. 10(a)], much smaller than required to depopulate a significant part of the ion beam.

These arguments leave electron-induced cooling [Eq. (3)] as the mechanism driving the evolution of the rotational states in the stored ion beam. It should be noted that the time scale for variations of the DR rate coefficient through the radiation field alone, as revealed by the starting points of the various cooling curves in Fig. 14, approaches several tens of seconds at later times after injection and probably reaches $\gtrsim 100$ s as revealed by the additional test described above, when electrons were switched off at times of 35–50 s. In connection with the radiative lifetimes shown in Fig. 4, this indicates a rotational distribution dominantly composed of levels with $J \lesssim 6$, i.e., rotational temperatures of $\lesssim 300$ K.

B. Assignment and time dependence of DR fragment imaging spectra

The DR fragment imaging spectra shown in Fig. 13 were taken under similar cooling conditions as the curve shown by open symbols in Fig. 15, using the same electron density $(5.5 \times 10^6$ cm$^{-3})$ although the ion-beam energy was reduced in order to enhance the fragment separation in the detector plane. The time slices of the three imaging spectra are marked by arrows in Fig. 15. In the following, we will first give a preliminary assignment of the structures in the imaging distribution from the latest time slice, enlarged in Fig. 16; then we will consider the time evolution of the individual signals in two regions of this distribution with a subdivision at the interparticle distance $D=7$ mm.

As stated earlier, the broad structure at $D<7$ mm in the projected distance distribution, marked as Region 1 in Fig. 16, can only arise from the DR of ions initially in vibrational states with $v \geqslant 3$, proceeding to products where one He atom emerges in an excited state with a principal quantum number $n \geqslant 3$. Vertical lines, grouped according to the initial levels with $v \geqslant 3$ in this region, indicate the end points of the expected shapes $P_{v0nn'}(D)$ [cf. Eq. (28)] for transitions from a given vibrational level to the different fine-structure terms of the He$(1s^2 \ ^1S)$+He$(1s3l)$ final channel. The assignment of the signal in region 2 ($7 < D < 16$ mm) is at this point ambiguous. The peak at 7–12 mm can be well described by reactions from the ion's vibrational ground state $(v=0)$ to final states with an excited He atom in $1s2s \ ^3S, 1s2s \ ^1S, 1s2p \ ^3P$ and $1s2p \ ^1P$. However, the peak structure can also be described by including substantial contributions from $v=1$. Moreover, to fully describe the tail to higher distances, some contributions from vibrational states $v \geqslant 3$ are certainly needed, as indicated in the figure. In Sec. V C below it will be argued that the major part of the signal in region 2 indeed must arise from transitions from $v=0$.

Figure 17(a) shows the time evolution of the integrated signals in region 1 and region 2, $\widetilde{N}_d^{R1}$ and $\widetilde{N}_d^{R2}$ after normalization to the detected number of one-body events $\widetilde{N}_s$. The
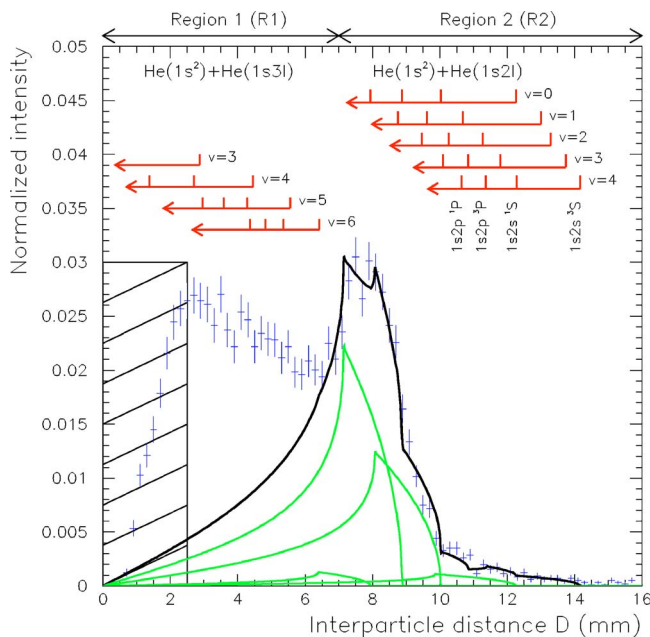
FIG. 16. (Color online) Assignment of DR reaction channels to the data of Fig. 13(d), taken at 10–22 s after injection. The vertical lines grouped for different intitial vibrational levels v show the end points of the distributions for various DR reaction channels as explained in the text. The black curve shows a least-squares fit to the data, explained in Sec. VI A; the gray lines show the contributions of the individual DR channels from $v=0$ included in this fit. The hatched area at low distance marks the region of limited detection due to overlapping light spots on the phosphor screen. Ion energy $E_i=3.36$ MeV; electron density $n_e=5.5\times10^6$ cm^{-3}.

signals from the two regions have very different time dependencies in the first ~6.5 s. While the signal from region 1 decreases strongly, the signal from region 2 shows a slight increase. From 6.5 s onwards both signals decrease, the signal from region 1 essentially reaching a constant level after ~12 s, while that from region 2 continues to decrease slowly over the full observation period up to 22 s. This tendency is emphasized in Fig. 17(b) where the ratio of the two signals, $\tilde{N}_d^{R1}/\tilde{N}_d^{R2}$, is displayed as a function of time. Thus the increase in the ratio at the late times demonstrates the different time evolution at times beyond >10 s.

The fact that the signals in regions 1 and 2 have very different time structures for the first 6.5 s proves that they originate from different parts of the rovibrational population in the ion beam at these times and indicates that the signal in region 2 arises from the lower vibrational levels, possibly up to $v=2$. This is also consistent with the fast vibrational stabilization, taking at most 12 s, imposed by the radiative decay of excited vibrational states as discussed in Sec. II C 2. The time evolution on the longer time scale (≥10 s) can be unambiguously assigned to rotational states with different DR cross sections. Since the signal from region 2 shows a time dependence after 10 s, while an apparent stabilization is seen for the signal in region 1 ($v\geq3$), the rotational dependence of the DR cross section seems to be more important for the vibrational ground state (possibly including $v=1$ and 2 which have not yet been excluded at this point) than for the higher vibrational states.
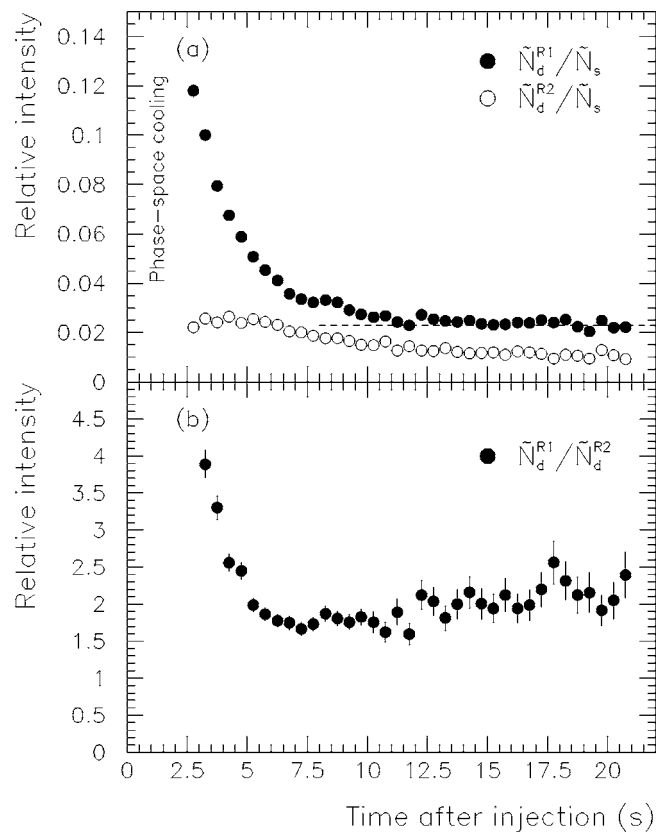

FIG. 17. Time evolution of the dissociative recombination signal at $E_d=0$ as observed with the fragment imaging technique (contribution from the central part of the electron cooler only). (a) Intensities of the signals from the regions 1 and 2 of the fragment imaging distribution (cf. Fig. 16) relative to the observed number $\tilde{N}_s$ of one-body imaging events. (b) Ratio of the signal intensities from regions 1 and 2.

The distribution of interparticle distances in Fig. 16 shows that vibrational levels with $v\geq3$ (region 1) contribute significantly to the DR signal even after >10 s of storage time, in contrast to the expected effect of radiative relaxation (Sec. II C 2), which would yield insignificant excited-state populations not contributing to the DR signal despite their predicted large cross sections. In consequence, since the populations cannot be determined by radiative interactions alone, the stored ions must experience vibrational excitation by some further mechanism(s).

C. Fragment imaging pump-probe experiments

The observations that the signal in region 1 arises from higher vibrational states ($v\geq3$) and that the major part of region 2 originates from DR of the lower vibrational states makes it possible to use a pump-probe-type experiment to investigate the effect of the electron beam and of residual-gas collisions on the vibrational population. The operation of the electron cooler during these measurements is schematically shown in Fig. 18(a). Following each injection, the energy of the electron beam is altered in a regular time pattern, spending several time intervals of 1 s each at an excitation energy [$E_d=4.0$ eV in Fig. 18(a)] and interrupting these ex-
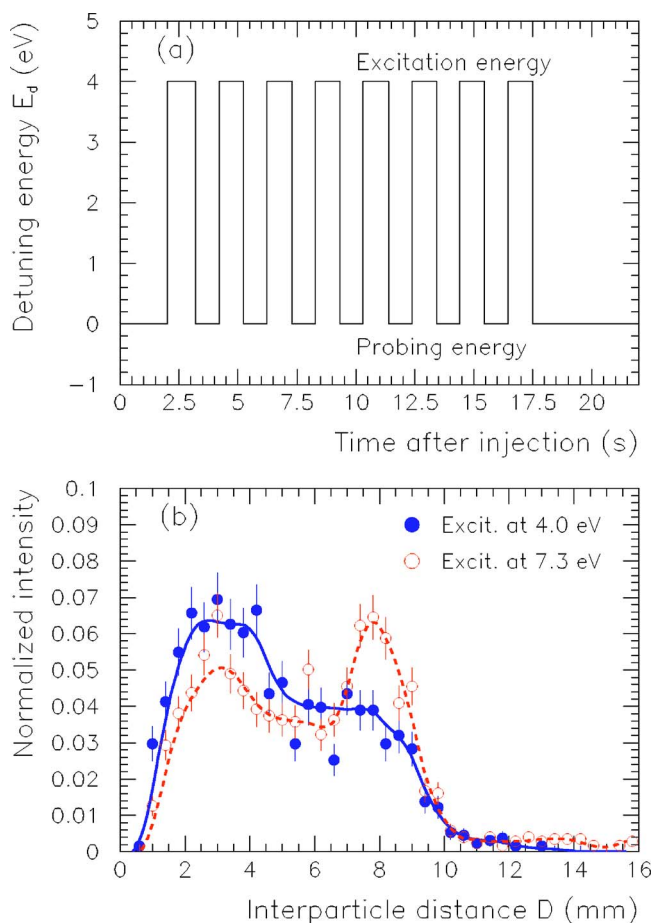
FIG. 18. (Color online) Pump-probe experiments using the fragment imaging method. (a) Schematic illustration of the operation of the electron cooler. (b) Projected distance spectrum obtained in the four probing periods within the time interval 9–16 s, each time following excitation with electrons at 4.0 eV (filled circles) and 7.3 eV (open circles). The shapes of the two distributions are emphasized (to guide the eye) by the solid and the dotted curves. Ion energy $E_i = 3.36$ MeV; electron density $n_e = 5.5 \times 10^6$ cm^{-3}.
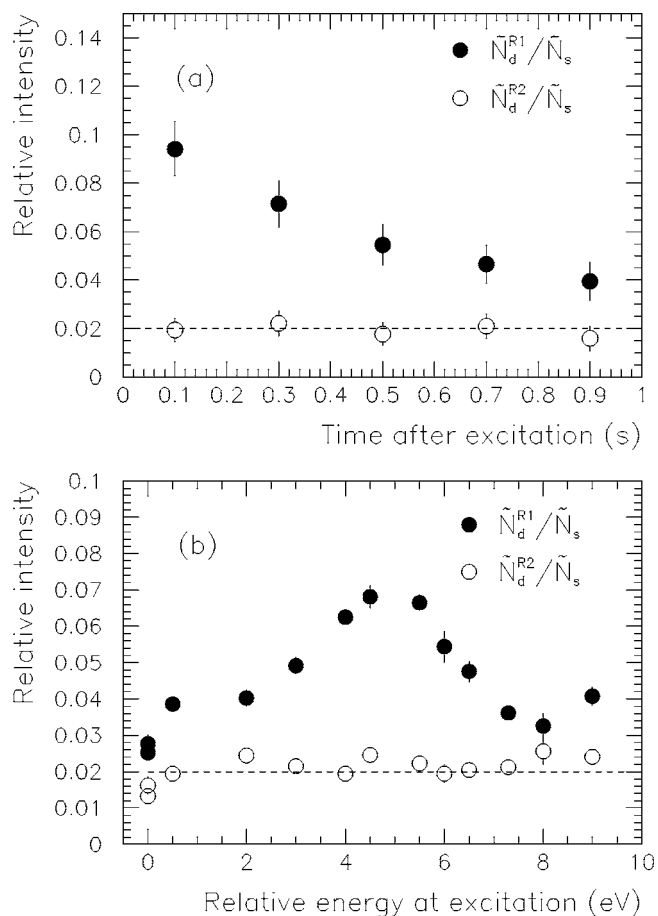
FIG. 19. Electron induced vibrational excitation as studied with the DR fragment imaging pump-probe experiments. The DR signals occurring in region 1 (filled circles) and region 2 (open circles) (cf. Fig. 16) are shown (a) as a function of time after excitation with electrons at 4 eV, and (b) as a function of the excitation energy. The counts were collected from the four probing periods for ≥ 9s after injection; the counts in regions 1 and 2 have been normalized to the observed number $\widetilde{N}_s$ of one-body imaging events.

citation periods by probing intervals of 1 s each, where projected fragment distance distributions are recorded at $E_d = 0$ (probing energy). The effect of electron excitation at different energies is illustrated in Fig. 18(b) by showing the distribution of projected distances accumulated in the last four probing intervals [$t = 9$–16 s, see Fig. 18(a)] at two different excitation energies. The ratio of events in the regions 1 and 2 is clearly different for the two excitation energies, region 1 (originating from $v \geqslant 3$) dominating the spectrum much more for 4.0-eV excitation than for 7.3-eV excitation.

In the following, we will quantify the DR rates associated with regions 1 and 2 by the integrated counts of two-body events in the respective regions, and , each normalized to the number $\widetilde{N}_s$ of single-hit events during the same counting period. Obviously, the signals in regions 1 and 2 are not completely independent since the reactions contributing to the signal in region 2 partly give intensity to region 1. However, it is evident from Fig. 17 that the signal in region 2 evolves slowly with time, and to a first approximation its contribution to region 1 can be considered constant. With this obser-

vation, the relative intensity for region 1 yields a useful probe signal for the vibrational population in $v \geqslant 3$, provided one keeps in mind that it contains an offset contribution proportional to the corresponding signal for region 2. It should also be stressed that, compared to the continuous operation used in Secs. V A and V B, the switching operation in the pump-probe measurements leads to somewhat different average effects of the electron beam on the rovibrational populations in the ion beam, so that the rates $\widetilde{N}_d^{R1,R2}/\widetilde{N}_s$ cannot be directly compared to the corresponding quantities of the previous measurements at the same storage times.

The association of region 1 with vibrationally excited ions is supported by observing the time dependence of the signal following the end of an excitation period. For this purpose, the data collected in the probing intervals are subdivided into time bins counting from the start of the probing period. The temporal variation of the signals from both regions after the end of excitation is shown for an excitation energy of 4 eV in Fig. 19(a). The DR signal from region 1 is enhanced right after the electron excitation period and then shows a signifi-

cant, rapid decrease. The time constant for the decay of this signal (containing a constant offset due to the contributions from region 2, as discussed above) is consistent with the expected radiative lifetime of the levels $v=3$–5, lying in the range of 0.4–0.25 s as shown in Fig. 4. Remarkably, no significant time variation (above a 10% level) is seen on the DR signal from region 2. The radiative lifetimes of all excited v levels (populated either directly or by the radiative cascade from $v \geqslant 3$) are short enough that significant contributions to the region-2 DR signal from such levels should reveal themselves by a decaying component in the time-dependent pump-probe measurement of Fig. 19(a). In combination with the results from the CEI, where the vibrational ground state was seen to dominate the ion beam after 3 s of storage, the absence of a time variation of the DR signal from region 2 thus provides a strong experimental evidence that the major part of this signal originates from the vibrational ground state ($v=0$). Furthermore, this results suggest that the DR rate coefficient from the $v=1$ and $v=2$ levels are not significantly higher then from the $v=0$ level.

It should also be noted that the constant value of [marked by a dashed line in Fig. 19(a)] is slightly higher than obtained at the same storage times when the electron beam at zero energy was applied continuously [Fig. 17(a)]. This is consistent with the interpretation of a strong electron induced rotational de-excitation at zero energy, as discussed in Sec. V A.

The variation of the vibrational excitation with the electron energy is displayed in Fig. 19(b). The signal from region 1 is clearly energy dependent with a peak at ~5 eV. The mechanism underlying this observed electron-induced vibrational excitation will be discussed in Sec. VI E. The signal originating from region 2 has no energy dependence, confirming again that this part of the DR signal originates predominantly from ^{3}He ^{4}He$^+$($v=0$) ions. Note that the energy range scanned in this measurement covers an essential part of the electron energies present in the toroid regions of the electron cooler when the detuning energy in the central part of the electron cooler is close to zero.

Fragment imaging measurements with a similar timing cycle were performed to probe the effect of leaving the ^{3}He ^{4}He$^+$ ions under the influence of residual gas collisions only. To this end, following each injection, the probing periods were again arranged as in Fig. 18(a), but instead of stepping up the electron energy the electron beam was switched off for 1 s between the probing periods. Figure 20 shows that under these conditions the probe signal from region 1 is essentially constant, possibly with a slight temporal increase showing the effect of vibrational excitation from the toroid regions after the electrons have been switched back on. The signal ratio between regions 1 and 2 during the probing period continuously stays at ~2, a value close to that found when the electron beam was continuously on [$t>9$ s in Fig. 17(b)]. Altogether, the dominant part of the observed vibrational excitation persists in the stored ^{3}He ^{4}He$^+$ beam even during the absence of the electron beam (over times that exceed the radiative lifetime of the excited vibrational levels). We conclude that the dominant role in maintaining a small nonthermal vibrational population in the stored beam is played by ion collisions with the residual gas.
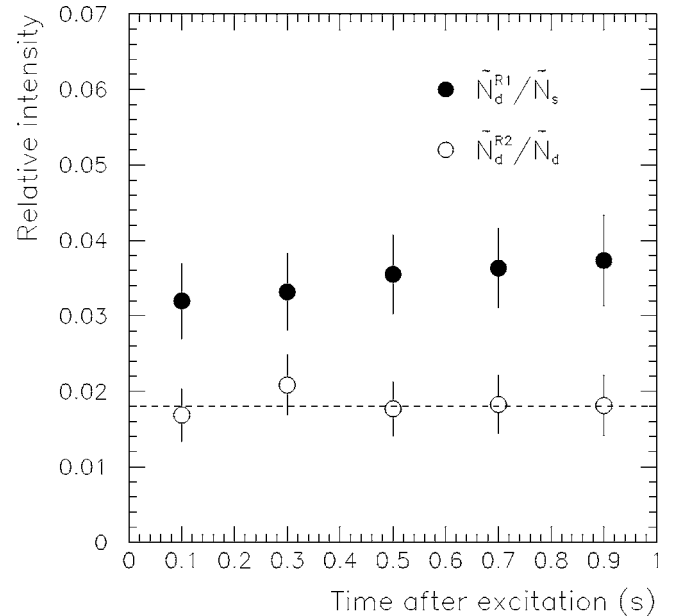

FIG. 20. Residual-gas induced vibrational excitation as studied with the fragment imaging pump-probe experiments. The DR signals occurring in region 1 (filled circles) and region 2 (open circles) (cf. Fig. 16) are shown as a function of time after turning on the electron beam again, following an off period of 1 s. The counts were collected and normalized as in Fig. 19.

VI. RESULTS

A. Low-energy DR: Initial-to-final-state dynamics

The absence of a time dependence of the rate in the pump-probe experiments of Sec. V C shows that at most ~10% of the signal in region 2 ($D>7$ mm) of the DR fragment imaging distributions at $E_d=0$ can arise from ^{3}He ^{4}He$^+$ ions in the vibrationally excited states. Hence the shoulders on the right-hand side of the fragments imaging distribution of Fig. 16 can be overwhelmingly assigned to different final states of ^{3}He ^{4}He$^+$($v=0$) DR. Consequently, the distribution was fitted with the individual initial-to-final-state contributions listed in Table I, yielding the full line in Fig. 16. In particular, the dominant contributions peaking at ~7.2 and ~8.0 mm (cf. Fig. 16) must come from the ^3P and ^1S states, respectively. Contributions to the imaging signal whose

TABLE I. Signal contributions (normalized to the integral of the observed distribution) obtained from a least-squares fit to the DR fragment imaging distribution at $E_d=0$, listed in the sequence of increasing kinetic energy release.

Initial state	Final channel	Contribution
^{3}He ^{4}He$^+$ ($v=0$)	He($1s^2$ ^1S)+He($1s2p$ ^1P)	0.0154(16)
^{3}He ^{4}He$^+$ ($v=0$)	He($1s^2$ ^1S)+He($1s2p$ ^3P)	0.311(28)
^{3}He ^{4}He$^+$ ($v=0$)	He($1s^2$ ^1S)+He($1s2s$ ^1S)	0.198(21)
^{3}He ^{4}He$^+$ ($v=3$)	He($1s^2$ ^1S)+He($1s2p$ ^3P)	0.041(14)
^{3}He ^{4}He$^+$ ($v=0$)	He($1s^2$ ^1S)+He($1s2s$ ^3S)	0.0196(6)
^{3}He ^{4}He$^+$ ($v=4$)	He($1s^2$ ^1S)+He($1s2s$ ^3S)	0.025(3)

TABLE II. Measured final-state branching ratios following low-energy DR from the $v=0$ level of ^{3}He ^{4}He$^+$.

Final channel	Branching ratio (%)
He$(1s^2\ ^1S)+$He$(1s2s\ ^3S)$	3.7 ± 1.2
He$(1s^2\ ^1S)+$He$(1s2s\ ^1S)$	37.4 ± 4.0
He$(1s^2\ ^1S)+$He$(1s2p\ ^3P)$	58.6 ± 5.2
He$(1s^2\ ^1S)+$He$(1s2p\ ^1P)$	2.9 ± 3.0

shape cannot be attributed to $v=0$ ions are on the few-percent level; within the remaining arbitrariness caused by the similarity of the energy release for the different channels with $v\neq0$, they were attributed to certain final states reached from ions with $v=3$ and 4, as indicated in Table I.

The fitted signal contributions of Table I now yield the branching ratios for DR of ^{3}He ^{4}He$^+(v=0)$ ions into the various fine-structure terms of the $n=2$ final atomic states. Table II lists these ratios, which show a dominance of the $1s2p\ ^3P$ and $1s2s\ ^1S$ fine-structure levels; this result will be further discussed in Sec. VII A 2.

In addition, it is possible to extract from Table I the fraction of all detected two-body events that originates from ^{3}He ^{4}He$^+$ in the vibrational ground state, which amounts to $\tilde{I}(v=0)=0.54(5)$. This result will be used in the next section to derive the low-energy DR rate coefficient for $v=0$ ^{3}He ^{4}He$^+$ ions.

The levels $v\geq3$ do yield a substantial DR signal in region 1 ($n\geq3$ final atomic states) but, remarkably, still seem to contribute very little to region 2. Hence ions in these levels show a strong preference for DR into the higher-lying atomic states, avoiding the $n=2$ final levels.

The low fraction (at most $\sim10\%$) of signal contributions from vibrationally excited ions in region 2 suggest that the rate coefficient from $v=1$ and 2, for which the DR can contribute to region 2 only ($n=2$ final atomic states), are not significantly higher than for $v=0$. This results is surprising since the DR rate coefficient was predicted in Ref. [10] to increase by at least a factor of 10 for each quantum of vibrational excitation between $v=0$ and 2 through the improving Franck-Condon overlap. The alternative explanation that the levels $v=1$ and 2 have a much smaller population in the ion beam than the levels with $v\geq3$ seems unlikely considering the propensity rule $\Delta v=1$ for the radiative cascade through the vibrational levels.

B. Absolute low-energy DR rate coefficient

From the comparison of the ion beam decay rate with and without the presence of the electron beam, an absolute rate coefficient of $\tilde{\alpha}_{DR}(E_r)=2.8(4)\times10^{-8}$ cm^3 s^{-1} was deduced in Sec. IV A 2 for the DR on the high-energy peak at a relative energy of $E_d^r=7.3$ eV. The energy-dependent rate measurements were normalized using this absolute rate and, after the toroid correction (see Sec. IV A 3), yield for $t>35$ s a zero-energy, rovibrationally averaged DR rate coefficient of $\tilde{\alpha}_{DR}(0)=2.7(4)\times10^{-9}$ cm^3 s^{-1}. Following the assignment and the fit of the DR fragment imaging distribution

as discussed in the previous section, it becomes possible to determine the fraction of the observed DR rate at $E_d=0$ that originates from $v=0$ ^{3}He ^{4}He$^+$ ions.

The total intensity in the fragment imaging spectrum, corresponding to the toroid-corrected averaged rate coefficient $\tilde{\alpha}_{DR}(0)$, is reduced by the limited detection, as discussed in Sec. IV B 2, by a factor of $1-\tilde{f}_d$, where $\tilde{f}_d$ was obtained in Eq. (30). The integrated intensity $\tilde{I}(v=0)$ of the fitted $v=0$ contributions in the normalized fragment imaging spectrum can therefore be written as

$$\tilde{I}(v=0)=\frac{p_0\tilde{\alpha}_{DR}^{v=0}(0)}{(1-\tilde{f}_d)\tilde{\alpha}_{DR}(0)}, \qquad (31)$$

using the effective contribution $p_0\tilde{\alpha}_{DR}^{v=0}(0)$ from $v=0$ ions contained in $\tilde{\alpha}_{DR}(0)$ as defined by Eq. (5). Within the error of the absolute rate coefficient scale of $\sim20\%$ we can here neglect the deviation of p_0 from unity.

Using the values of $\tilde{I}(v=0)$ and $\tilde{\alpha}_{DR}(0)$ determined above, we then obtain

$$\tilde{\alpha}_{DR}^{v=0}(0)=(7.3\pm2.1)\times10^{-10}\ \text{cm}^3\ \text{s}^{-1}. \qquad (32)$$

This rate coefficient is still *averaged* over the relaxed rotational distribution resulting after storage and electron cooling of 35 s (cf. Sec. V A). The influence of the rotational relaxation is illustrated by the open symbols in Fig. 15, keeping in mind that the given result was obtained with an electron density of 5.5×10^6 cm^{-3}.

Assuming a DR cross section varying as $\propto E^{-1}$ up to ~0.1 eV, the merged-beams rate coefficient $\tilde{\alpha}_{DR}^{v=0}(0)$ can be converted to a rate coefficient for a thermal, isotropic electron velocity distribution at 300 K through the division by a factor of $(300\ \text{K}/T_\perp)^{1/2}$ arctan $(T_\perp/T_\parallel-1)^{1/2}/(1-T_\parallel/T_\perp)^{1/2}$ $=2.2$ that follows from the respective averages over isotropic and anisotropic Maxwellians. This yields $\tilde{\alpha}_{300\ \text{K,DR}}^{v=0}$ $=(3.3\pm0.9)\times10^{-10}$ cm^3 s^{-1}.

After subtraction of $\alpha_{DR}^{v=0}(0)$ from the total observed rate coefficient $\tilde{\alpha}_{DR}(0)$, a difference of $\Delta\tilde{\alpha}_{DR}(0)$ $=1.9(5)\times10^{-9}$ cm^3 s^{-1} remains, that represents the fraction due to vibrationally excited ions in states $v\geq3$. The value of $\Delta\tilde{\alpha}_{DR}(0)$ can be used to estimate the zero-energy DR rate coefficient for excited vibrational states $v\geq3$. Assuming relative populations $p_v=\Sigma_J p_{vJ}<0.01$ for these levels, we obtain $\tilde{\alpha}_{DR}^{v\geq3}(0)\gtrsim2\times10^{-7}$ cm^3 s^{-1}.

On the other hand, if a value of $\sim10^{-6}$ cm^3 s^{-1} is regarded as an upper limit for the DR rate coefficient of He$_2^+$ ions in any vibrational excited level, the relative population of levels with $v\geq3$ must be $\geq0.19\%$. Hence it is reasonable to assume excited vibrational states to occur in the stored ion beam at fractions between ~0.1 and 1 %.

C. Low-energy structure of the DR cross section

In the low-energy range the measured rate coefficient $\tilde{\alpha}_{DR}(E_d)$ shows a strong variation with time as illustrated for $E_d=0$ in Fig. 14. The measured energy dependence in two characteristic time windows is shown in Fig. 21. As discussed, contributions from higher vibrational states are sig-
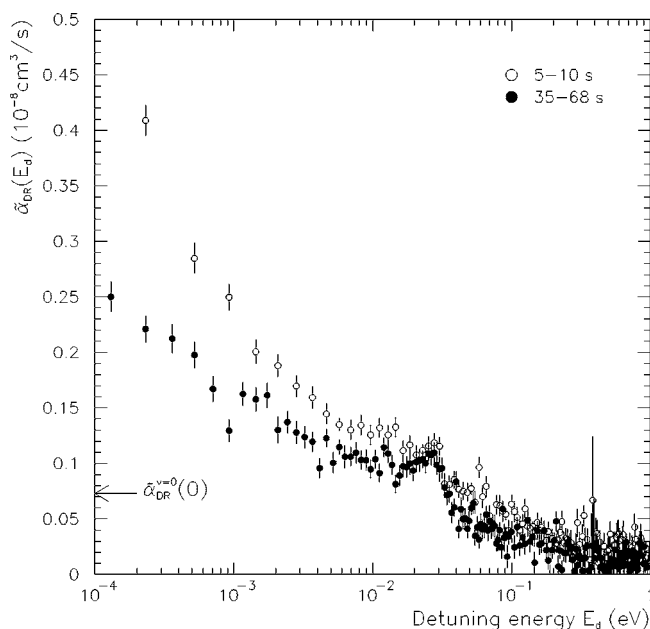
FIG. 21. Detailed view of the measured toroid corrected rate coefficients $\tilde{\alpha}_{DR}(E_d)$ at low relative energies obtained for storage time intervals of 5–10 s (open circles) and 35–68 s (filled circles); see Fig. 10(a) for a full view.

nificant even at long storage time, as illustrated by the indicated size of $\alpha_{DR}^{v=0}(0)$. The observed low-energy DR rate coefficient displays a peaklike structure at ~0.025 eV which persists over all accessible times after injection, but sharpens at the later times. The present measurement shows no indication of further structure in the DR cross section in the energy range below 1 eV.

D. High-energy structure of the DR cross section

At high collision energies, the variation of the rate coefficient $\tilde{\alpha}_{DR}(E_d)$ directly reflects the energy dependence of the DR cross section. The electron energy spread (~0.23 eV at 10 eV and ~0.34 eV at 20 eV) is small compared to the observed structures, so that the DR cross section $\tilde{\sigma}_{DR}(E)$ can be obtained directly from the rate coefficient using the relation $\tilde{\alpha}_{DR}(E_d) \sim (2E_d/m)^{1/2}\tilde{\sigma}_{DR}(E_d)$. The high-energy structure of the measured rate coefficient (Fig. 22) shows much less variation with the storage time, indicating that the sizes of the state-specific cross sections are similar to each other. Between 3 and 12 eV, a broad peak structure is observed that, as shown in Fig. 22(a), slightly shifts and narrows with time, again reflecting the evolution of rovibrational states in the beam during storage. The position and the width of this structure match well the energies of vertical transitions from the ionic vibrational ground state to dissociating neutral Rydberg states which converge to the repulsive $A\,^2\Sigma_u^+$ ionic state shown Fig. 1. The DR cross section arising from this reaction channel is found to be $(1.7\pm0.2)\times10^{-16}$ cm^2 at the peak near 7.3 eV.

At higher energies ($>$15 eV) the measured rate coefficient displays a rich structure with a small narrow peak (FWHM ~2 eV) at ~19 eV, a larger and broader peak at
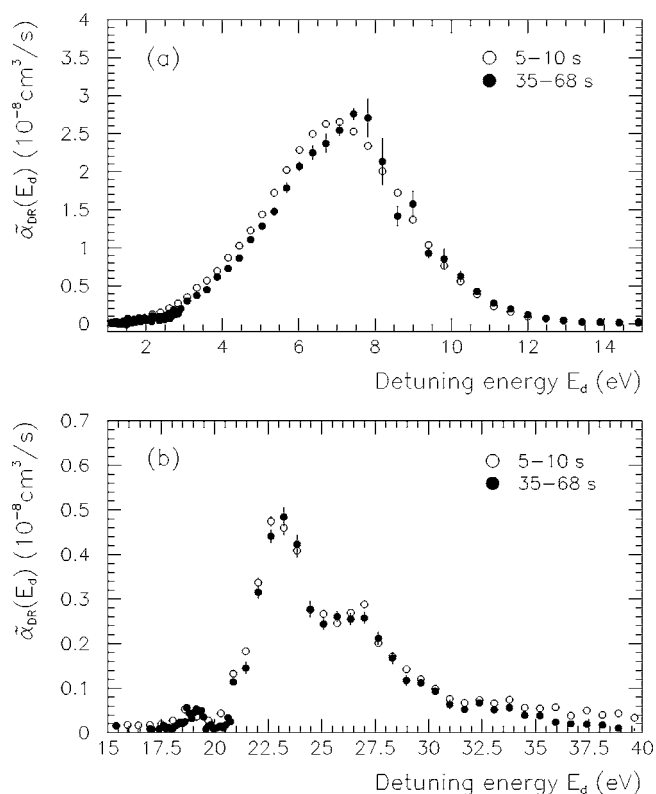

FIG. 22. Detailed view of the measured toroid corrected rate coefficients $\tilde{\alpha}_{DR}(E_d)$ obtained for storage time intervals of 5–10 s (open circles) and 35–68 s (filled circles) in the detuning energy ranges of (a) E_d=1–15 eV and (b) E_d=15–40 eV.

~22.5 eV, a plateaulike behavior at 25–27 eV, and a small modulation at 31 eV before the rate declines. In the energy region of these observed structures, vertical transitions from the ionic vibrational ground state can reach dissociating neutral Rydberg states attached to highly excited states of the He$_2^+$ ion; the ionic curves correlated to the He$^+$(1s)+He(1s2l) atomic limits are shown in Fig. 2. For instance, the energetic limit for dissociation into He(1s2s)+He(1snl)($n\geq2$) is 17.4 eV, and the peak at ~19 eV could well represent dissociation to these final states following an initial vertical electron capture process. Similarly, the energetic limit for dissociation into He(1s3l)+He(1snl)($n\geq3$) is 23.6 eV, for He(1s4l)+He(1snl)($n\geq4$) 25.0 eV, while the energetic limit for He$^+$(1s)+He$^+$(1s) is found at 26.9 eV. The very detailed structure, in particular the narrow peak at ~19 eV, may indicate the importance of individual core excited resonances as in the case of CD$^+$ [62].

E. Energetic structure of DE and electron-impact vibrational excitation

In the present experiment, all three types of electron-induced reactions discussed in Sec. I were studied as a function of the collision energy. For the energy range of vertical transitions from the ionic ground state to neutral dissociating Rydberg states attached to the lowest excited state of He$_2^+$(~3–10 eV) the measured reaction rate coefficients for
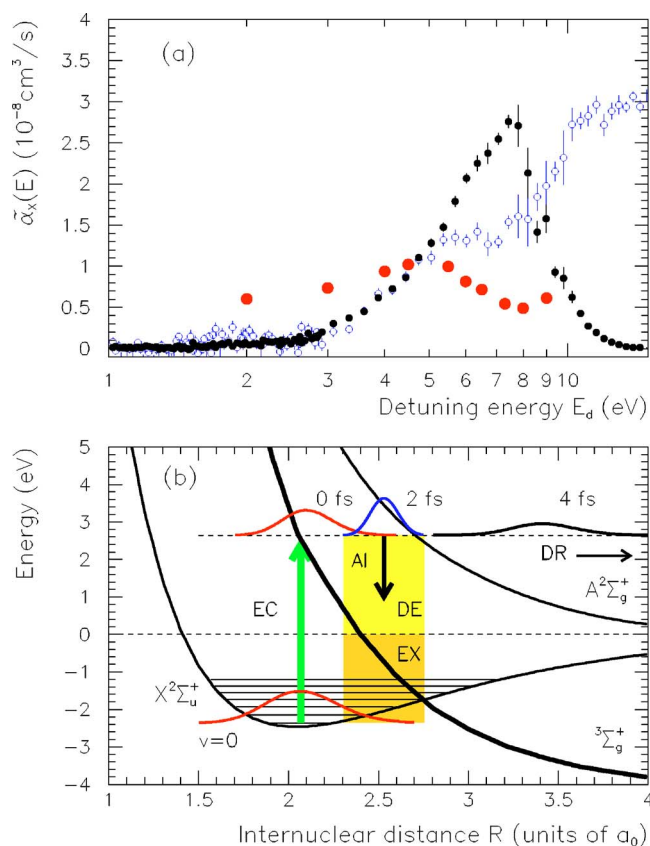
FIG. 23. (Color online) (a) Measured rate coefficients for DR (black filled circles) and DE (open circles) at t=35–68 s together with the vibrational excitation profile as obtained from the pump-probe experiments (light filled circles). The absolute scale of the excitation profile is arbitrarily chosen to compare its shape to the rate coefficients for DR and DE. (b) Schematic illustration (inspired by Ref. [63]) of the DR, DE, and vibrational excitation (EX) processes following an initial electron capture (EC) at 5 eV from the vibrational ground state (v=0) into the $^3\Sigma_g{}^+$ dissociative Ryberg state. Immediately after electron capture a nuclear wave packet (marked 0 fs) is formed in the $^3\Sigma_g{}^+$ potential, where it is repelled towards larger internuclear distances as illustrated by the wave packets at 2 and 4 fs; a process that finally leads to DR. During repulsion, the wave packet loses intensity since the molecule can autoionize (AI) to the ionic ground state, leading to either DE or EX. The gray shaded areas show the Frank-Condon region for electron reemission for the wave packet at 2 fs.

DE and DR are compared in Fig. 23(a). The energy dependence of the signal for electron-impact vibrational excitation to states $v \geqslant 3$, as obtained from the pump-probe measurements, is also included in Fig. 23(a). The absolute scale of the excitation profile is arbitrarily chosen in order to compare its shape to the rate coefficients for DR and DE.

Considering only the "direct" DE caused by simple electron impact excitation to the repulsive curve of He$_2{}^+$, the DE cross section should rise only at $\gtrsim 5$ eV (cf. Fig. 1). Here, we observe that the DE rate coefficient rises already at much lower energies, close to the dissociation threshold of ~ 2.4 eV, and indeed follows the energy dependence of the DR rate coefficient up to ~ 5 eV. Above this energy, the DE rate ceases to rise until the onset of the direct DE at ~ 7 eV,

which leads to a strong increase towards higher energies, while the DR rate drops. The DE signal below ~ 7 eV clearly shows the influence of intermediate neutral Rydberg states on this process. The vibrational excitation signal also occurs below the dissociation threshold and it extends far above the dissociation energy with a peak at ~ 5 eV. The peak position matches the vertical transition energy from the ionic ground state to the first neutral dissociative curve $^3\Sigma_g{}^+$ [see Fig. 23(b)], but also the higher-lying neutral states below the $A\,^2\Sigma_u{}^+$ ionic state appear to contribute. A similar excitation profile was previously reported for HD$^+$ [47,52]. The results underline the importance of the electronically doubly excited states in all, DR, DE, and electron-impact excitation of He$_2{}^+$ [53].

A mechanism of resonance enhanced DE and vibrational excitation was described by Orel and Kulander [63] for HeH$^+$. A similar mechanism is illustrated in Fig. 23(b) for He$_2{}^+$ involving the first $^3\Sigma_g{}^+$ Ryberg state reached vertically at 5 eV above the vibrational ground state. Following resonant capture of the incident electron, the resonance state autoionizes with a considerable fraction of the excitation energy being given to the nuclear motion, leading either into the vibrational continuum (DE) or into a bound vibrational state (EX) of the He$_2{}^+$ ion in its electronic ground state. DR results if the resonance evolves without autoionization.

VII. DISCUSSION

A. ^{3}He ^{4}He$^+$ DR

1. DR rate coefficient

Our general observations regarding the DR rate coefficient of ^{3}He ^{4}He$^+$ and its dependence on the ion storage time are in overall agreement with those of the only earlier storage ring experiment at ASTRID [31], which also showed a strong variation of the low-energy DR rate during the vibrational relaxation and indicated a small rate coefficient for the vibrational ground state. Very recently, absolute rates from this experiment were presented [64]. For low-energy DR, a thermal rate coefficient of $(6 \pm 3) \times 10^{-10}$ cm^3 s^{-1} for 300 K was extracted from the data at $\gtrsim 12$ s of storage time, including all possible contributions from excited rovibrational states of the stored ions. Within the statistical errors, the fragment imaging distributions from this experiment, also reported recently [64], do not show any contribution of the n=2 final atomic states, unlike the present data (cf. Sec. IV A). Hence the extraction of a rate coefficient for v=0 ions is not possible there; moreover, this may indicate a higher internal excitation of the stored ions than in our case. Converting our zero-energy, rovibrationally averaged DR rate coefficient $\tilde\alpha_{\mathrm{DR}}(0)=2.7(4) \times 10^{-9}$ cm^3 s^{-1} to a 300-K thermal value through the division by 2.2 (see Sec. VI B), we obtain—as a quantity equivalent to the rovibrationally averaged ASTRID result—a value of 1.2×10^{-9} cm^3 s^{-1}, significantly higher in spite of probably a lower internal excitation of the ions. Regarding high-energy DR, we find a significantly larger cross section than ASTRID on the peak near 7 eV [$1.7(2) \times 10^{-16}$ cm^2 (see Sec. VI D) vs $0.6(3) \times 10^{-16}$ cm^2 at ASTRID]; in addition, different values are

found for the position of the maximum (7.3 eV vs 6.6 eV at ASTRID). While some of these discrepancies may be explained by the different ion source and storage conditions in the two experiments, the reasons for the apparent disagreement in the absolute cross section, particularly obvious for the high-energy peak, are presently unknown.

For the vibrational ground state, our thermal DR rate coefficient of $\tilde{\alpha}_{300\ \mathrm{K,DR}}^{v=0}=(3.3\pm0.9)\times10^{-10}$ cm^3 s^{-1} is consistent with the limit of $<5\times10^{-10}$ cm^3 s^{-1} obtained by Deloche *et al.* [12]. For excited vibrational states, the result of $\tilde{\alpha}_{\mathrm{DR}}^{v\geq3}(0)\gtrsim2\times10^{-7}$ cm^3 s^{-1} (Sec. VI B), corresponding to thermal rate coefficients of $\gtrsim1\times10^{-7}$ cm^3 s^{-1}, clearly exceeds the limit of Ref. [12]. However, the observed strong increase of the DR rate coefficient for excited vibrational states is in accord with the measurement by Ivanov *et al.* [19] and with the calculations by Carata *et al.* [10].

Our low-energy thermal rate coefficient for the vibrational ground state is about a factor of 6 larger than the theoretical result $(6.1\times10^{-11}$ cm^3 s$^{-1})$ of Carata *et al.* [10] which, although given for $J=0$, differs only little from that for a rotational temperature of 300 K (see Fig. 14 of Ref. [10]) which should describe the present experimental conditions more adequately. Carata *et al.* emphasize [10] that nonadiabatic couplings to singly excited neutral states are not included in their calculation, so that the larger rate coefficient observed here may indicate the presence of such couplings (however, possible branching to ground-state He atoms [10] can be excluded experimentally as discussed in the following section).

Very recently, Royal and Orel [65] have obtained results for the high-energy DR of ^{3}He ^{4}He$^+(\sim2$–13 eV) using time-dependent wave-packet calculations. Their peak cross section of 7.5×10^{-17} cm^2 is significantly smaller than our result; the peak position is in good agreement, while the calculated peak shape does not reproduce the asymmetry found in our data for $t>35$ s (see Fig. 22, and Fig. 3 of Ref. [65]). The latter observation may indicate the presence of mechanisms or dissociating curves not included in the calculation.

2. DR branching ratios

To the best of our knowledge, previous experimental results regarding the final-state branching ratios for the low-energy DR of $v=0$ He$_2^+$ ions suitable for a comparison with our results are not available. Carata *et al.* [10] in their calculations found the $^3\Sigma_g^+$ curve to be the dominant dissociation route for the vibrational ground state. Although this curve diabatically correlates to the $1s2s\ ^3S$ final atomic state, we find only $\sim3.7\%$ of the DR events from the vibrational ground state in this channel (see Table II). The experimentally strongest channels (^3P and ^1S) correspond to dissociating curves yielding only minor contributions to the calculated DR rate [10]. The discrepancy with the results of these calculations indicates the presence of nonadiabatic couplings [66,67], which were not included in the theory, but suspected [10] to possibly cause an additional flux of dissociation to energetically lower asymptotic channels, notably to the ground-state product-channel He$(1s^2)$+He$(1s^2)$. From our DR fragment imaging results, we can with high sensitivity

exclude the presence of this channel, which for our experimental parameters would have a maximum interparticle separation of 37.2 mm and thus be easily recognizable on the 80-mm-diameter fragment imaging detector. In fact, also in the case of HeH$^+$ DR, characterized by strong nonadiabatic coupling, ground-state products could be excluded with high experimental sensitivity [68].

The small contribution from higher vibrational states in region 2 of the fragment imaging distributions (see Sec. IV A) is remarkable. Consequently, the strong DR from excited vibrational levels ($v\geq3$) proceeds mostly to final states with an excited He(nl) atom with $n\geq3$. Similar strong preferences for DR into the highest energetically open final channels were observed previously for the DR of HeH$^+$ [68] and LiH$^+$ [69].

B. Rovibrational excitation and de-excitation mechanisms and rates

1. Vibrational excitation of stored ^{3}He ^{4}He$^+$ ions

Using the coupled set of Eqs. (16) for the rovibrational populations in the stored ion beam, we have modeled the effect of inelastic collisions of the stored ions with residual gas molecules acting in addition to the blackbody-induced radiative transitions already discussed in Sec. II C. Lacking measurements or calculations suitable for a realisic modeling of MeV collisions between molecular ions and H$_2$ (the main component of the residual gas), we strongly simplify the case, using a single fixed cross section to describe the probability that the state v,J of a molecular ion is changed in a residual gas collision to a different state v',J with a certain $v'\neq v$. The same partial cross section σ_{inel}^g is used for all possible final v' within a model containing six vibrational levels ($v=0$–5) and 30 rotational levels ($J=0$–29). Since the relevant collisions, leaving the molecular ion intact in spite of the high collision energy, are likely to proceed at large distance with a small exchange of momentum, we assume that the rotational quantum number is preserved. We then obtain rate constants k_{inel}^g according to Eq. (11) with $n_g=1.3\times10^6$ cm^{-3} and include the term

$$+\sum_{v'}(k_{\mathrm{inel}}^g N_{v'J}-k_{\mathrm{inel}}^g N_{vJ}) \qquad (33)$$

on each of the right-hand sides of Eqs. (16), thus describing the collisional excitation and de-excitation of vibrational levels in residual gas collisions. As expected (see Sec. II C) the equilibrium under the influence of residual gas collisions was always reached faster than under the action of radiative transitions alone (Fig. 5). The equilibrium populations obtained in competition with radiative relaxation for four different values of σ_{inel}^g are shown in Fig. 24. The excited-state equilibrium populations on the order of 1% indicated by the experimental results are found to correspond to partial inelastic collision cross sections of the order of a few 10^{-18} cm^2.

From the ion-beam decay rate k_{DE}^g (see Sec. IV A 2) the partial cross section for each of the two DE reaction channels in a residual gas collision [Eq. (9)] is determined to be 2.7×10^{-17} cm^2. On the other hand, the cross section for dis-
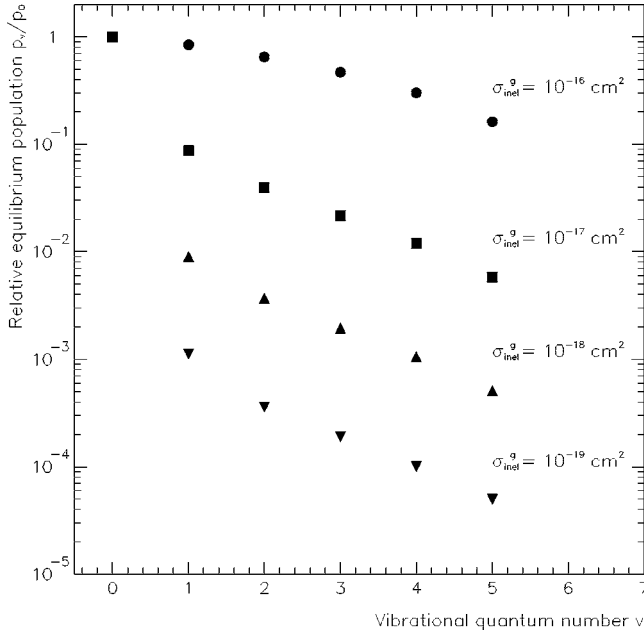
FIG. 24. Calculated vibrational equilbrium populations p_v, relative to the population p_0 in $v=0$, obtained when vibrational excitation through collisions with the residual gas [Eq. (33)] is included in the model of Eqs. (16) for four values of the excitation cross section σ_{inel}^g as indicated. Six vibrational levels ($v=0$–5) and 30 rotational levels ($J=0$–29) on each vibrational level are modeled; the residual gas density is set to $n_g=1.3\times10^6$ cm^{-3} and the temperature of the radiation field to 300 K.

sociative charge exchange [Eq. (10)] is found to be 4×10^{-20} cm^2. The estimated vibrational excitation cross sections lie between both values. The reaction mechanism(s) that can lead to vibrational excitation of the stored ions after collisions with a residual gas molecule (H$_2$) at MeV energies is not obvious. It may proceed as a direct vibrational excitation reaction or it may proceed as a relaxation process after an initial charge exchange collision. Clearly, to understand better the importance of the vibrational excitation in storage ring measurements, there is a need for theoretical work on such processes both in view of obtaining absolute cross sections and understanding the underlying mechanisms.

The result shows that for molecular ions that are not or only weakly radiatively active (unlike ^{3}He ^{4}He$^+$), an ion beam stored in a storage ring may stabilize with a significant vibrational excitation, even though the molecules may have been produced vibrationally cold in the ion source. However, in the well studied case of stored H$_2^+$ ions, electron-induced vibrational de-excitation turned out to be a strong process [50] and found to dominate the stabilized level of vibrational excitation.

2. Rotational excitation and cooling

The interaction with electrons at zero detuning energy ($E_d=0$) was shown in Sec. V A to have a strong effect on the DR rate coefficient $\tilde{\alpha}_{\mathrm{DR}}(0)$, as represented by the time dependence of the normalized DR rate $R_{(7)}/R_{(3)}$. While the evolution $\lesssim10$ s was attributed mainly to vibrational stabiliza-

tion, the time scale of the observed variations beyond 10 s was assigned to changes in the relative rotational level populations within the vibrational ground state. Here we address the time dependence of the normalized DR rate $R_{(7)}/R_{(3)}$ beyond 10 s by exploring possible mechanisms changing the rotational populations in the stored ion beam in a similar way as in the previous subsection, extending the set of Eqs. (16) and following the resulting time evolution in a model calculation. A complete modeling of the normalized DR rate $R_{(7)}/R_{(3)}$ is excluded considering that the detailed rate coefficients $\alpha_{\mathrm{DR}}^{vJ}$ (possibly with strong resonances for certain J's) are unknown. With the aim of illustration, we focus mainly on the time dependence of the rotational temperature for an ensemble of ions, since the time scale of changes in the normalized DR rate $R_{(7)}/R_{(3)}$ still qualitatively reflects the time scale of changes in the rotational temperature, despite a complicated J dependence of $\alpha_{\mathrm{DR}}^{vJ}$.

As discussed in Sec. V A, a rotational dependence of the DR rate coefficient might lead to selective depletion of excited rotational levels, provided the involved rate coefficients are large enough. To schematically investigate this effect, we parametrize the DR rate coefficient as

$$\alpha_{\mathrm{DR}}^{vJ}(0) = a_v(1 + bJ), \tag{34}$$

where the parameter a_v represents the vibrational and b the rotational dependence. The v- and J-dependent DR rates are included by adding the terms

$$- k_{\mathrm{DR}}^{vJ}(0)N_{vJ} \tag{35}$$

to the right-hand sides of Eqs. (16). The increase of the DR rate with the vibrational level was included by choosing $a_0 =5\times10^{-10}$ cm^3 s^{-1} and letting a_v increase by a factor of 10 for each consecutive excited state up to $v=3$, and then setting $a_v=5\times10^{-7}$ cm^3 s^{-1} for $v\geq3$. A strong J-dependent increase of $\alpha_{\mathrm{DR}}^{vJ}(0)$ was assumed with $b=1$. As before, a model with six vibrational levels ($v=0$–5) was considered. In comparison to radiative relaxation alone [Fig. 25(a), curve α], the inclusion of DR depletion (curve β) has a small effect as long as the vibrational excitation in residual gas collision is neglected (depletion is only efficient at short times, when excited vibrational levels are still significantly populated). If the population of excited vibrational levels by residual gas collisions is included, adding the terms of Eq. (33), the depletion effect tends to become stronger; however, a time scale of the cooling effect comparable to that observed in Fig. 14 is reached only for very large values of σ_{inel}^g, for which excited vibrational states would be about as strongly populated as the $v=0$ ground state. This situation is not found in the experiment and hence, as already stated in Sec. V A, depletion [even with the strong effect implied by choosing $b=1$ in Eq. (34)] cannot lead to significant changes of the rotational temperature on the time scales of the electron-induced cooling effect of Fig. 14.

To estimate the effect of rotationally inelastic electron collisions [Eq. (3) with $v=v'$] we parametrize the rotational excitation cross section, inspired by the formulation given by Rabadan *et al.* [54], as

$$\sigma_{\text{EX}}^{J \to J'}(E) = \sigma_0 \sqrt{\frac{E - E_{J'}^J}{E} \frac{E_{J'}^J}{E}}, \qquad (36)$$

where the overall size of the cross section is determined by the parameter σ_0. The corresponding de-excitation cross section is derived from the principle of microscopic reversibility, and written as

$$\sigma_{\text{DEX}}^{J' \to J}(E') = \sigma_{\text{EX}}^{J \to J'}(E' + E_{J'}^J) \sqrt{\frac{E' + E_{J'}^J}{E'}} \frac{2J + 1}{2J' + 1}. \quad (37)$$

The rotationally inelastic electron collisions are then included in the coupled set of Eqs. (16) by adding the following terms to its right-hand side:

$$+ \sum_{(vJ') > (vJ)} \left[k_{\text{DEX}}^{J' \to J}(0) N_{vJ'} - k_{\text{EX}}^{J \to J'}(0) N_{vJ} \right],$$

$$+ \sum_{(vJ') < (vJ)} \left[k_{\text{EX}}^{J' \to J}(0) N_{vJ'} - k_{\text{DEX}}^{J \to J'}(0) N_{vJ} \right], \qquad (38)$$

where $k_{\text{EX}}^{J \to J'}(E_d)$ and $k_{\text{DEX}}^{J \to J'}(E_d)$ are defined according to Eq. (12). Figure 25(b) illustrates the effect of the electron induced rotational transitions for two different values of σ_0 in comparison to the case where only radiative transitions affect the rotational population. For simplicity, the electron-induced transitions included in the model were restricted to $\Delta J = \pm 1$.

This calculation indicates that significant changes of the rotational temperature on the time scales of the observed cooling effect in Fig. 14 can be obtained by electron-induced rotational transitions for σ_0 of the order of 10^{-12} cm^2; the collisional cooling in fact leads down to the electron temperature $(kT_\perp = 10 \text{ meV}, T_\perp = 116 \text{ K})$ which is included through the averaging of the excitation and de-excitation cross sections according to Eq. (12). The required value of the cross section constant σ_0 (amounting to $\sim 10^4$ Å^2) is not unrealistic [55] and slightly smaller values may in fact be sufficient if transitions other than $\Delta J = \pm 1$ [54] are considered in addition. Figure 26 displays calculated ratios $R_{(7)}/R_{(3)}$ as a function of time both when the rotational de-excitations are negligible (solid line) and when they have a strong effect on the rotational temperature (dashed lines). Even with the simplifying assumptions made here, the model calculation in Fig. 26 reproduces almost quantitatively the experimental data of Fig. 14 when a strong rotational de-excitation is included.

Summarizing, the model calculations—in combination with the finding of only small populations on the percent level in excited vibrational states—suggest that the observed temporal evolution of the low-energy DR signal of stored ^{3}He ^{4}He$^+$ ions is due to rotational cooling through inelastic electron collisions, and not due to the combined action of DR depletion and vibrational excitation.

Rotational excitation and de-excitation in electron collisions have already been considered theoretically for several molecular ions (see, e.g., Ref. [54]). It must be expected that such reactions play a significant role for other storage ring measurements on DR too. In a study of D$_2$H$^+$ [48] a similar time dependence of the low-energy DR rate was observed, in
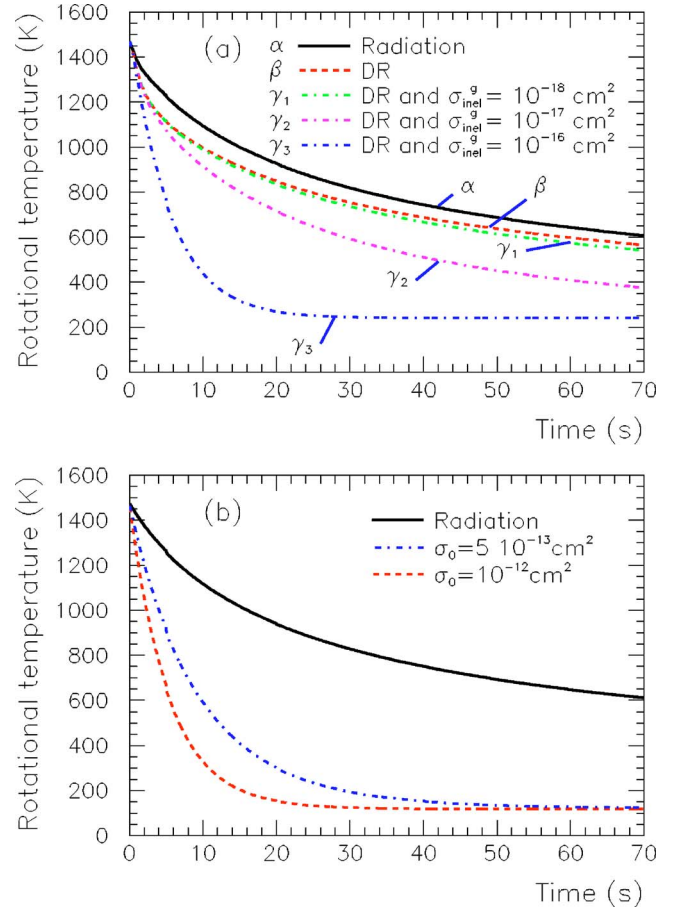

FIG. 25. (Color online) Calculated effects of electron-ion collisions and ion-residual gas collisions on the rotational thermalization in the $X^2\Sigma_u^+$ electronic ground state of ^{3}He ^{4}He$^+$ from an initial temperature of 1500 K. (a) Influence of (α) radiative transitions (solid), (β) radiation and DR depletion [Eqs. (34) and (35); dashed], and (γ_{1-3}) radiation, DR depletion, and vibrational excitation in the residual gas [Eq. (33)] with different excitation cross sections σ_{inel}^g (dotted). Initially, the six lowest vibrational levels were populated equally, with a rotational temperature of 1500 K imposed on each level. The electron density was set to $n_e = 1.2 \times 10^7$ cm^{-3} and the residual gas density to $n_g = 1.3 \times 10^6$ cm^{-3}. (b) Influence of radiative transitions (solid) and of radiation plus rotationally inelastic collisions in the velocity-matched electron beam [Eqs. (36)–(38)]. The cross section constant was set to $\sigma_0 = 5 \times 10^{-13}$ cm^2 (dash-dotted) and 10^{-12} cm^2 (dashed). Initially, only the vibrational ground state was assumed to be populated with a rotational temperature of 1500 K. The experimental electron temperatures were used to derive the rate coefficients of the inelastic electron collisions; n_e as in (a).

that case with a considerably large DR rate coefficient, so that the observed changes of rotational populations were attributed mainly to selective ion depletion by DR from the ion beam, implying a linear dependence of the rate coefficient on the rotational temperature with slope 0.94×10^{-9} cm^{3}s^{-1}K^{-1}. However, additional de-excitation of D$_2$H$^+$ ions by rotationally inelastic electron collisions could not be excluded, as also in this case the actual dependence of the DR rate coefficient on the rotational level is still unknown.
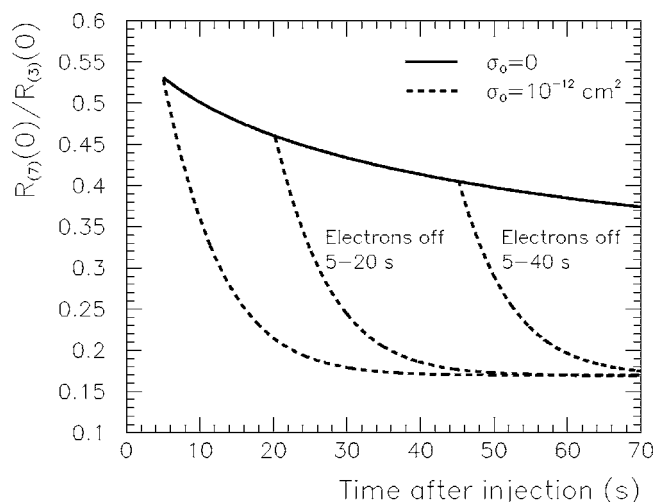
FIG. 26. Model calculation of the observable ratio $R_{(7)}/R_{(3)}$ including the effect of radiation, DR depletion, and rotationally inelastic collisions. Only the vibrational ground state $v=0$ was populated and it was assumed that a rotational temperature of 1500 K was reached after 5 s of ion storage. The electron density was $n_e = 1.2 \times 10^7$ cm^{-3}. $R_{(7)}$ was obtained using the model rate coefficient of Eq. (34) with $a_0 = 5 \times 10^{-10}$ cm^2 s^{-1} and $b=1$. $R_{(3)}$ rate was calculated as $[f_g k_{DE}^g + \tilde{k}_{DE}(0)] \times N_i$, with $f_g = 0.044, k_{DE}^g = 0.0506$ s^{-1}, and $\tilde{k}_{DE}(0) = 8.73 \times 10^{-4}$ s^{-1}. The solid curve shows the ratio $R_{(7)}/R_{(3)}$ when the rotationally inelastic collisions are neglected ($\sigma_0 = 0$). The dashed curves show the ratio $R_{(7)}/R_{(3)}$ computed with a strong electron induced rotational de-excitation ($\sigma_0 = 10^{-12}$ cm^2) with the electron beam being either continously on or switched off for time intervals of 5–20 s and 5–40 s as marked.

VIII. CONCLUSION

The present merged-beams DR measurements with ^{3}He ^{4}He$^+$ ions clearly confirm the predicted strong dependence of the DR cross section for He$_2^+$ on the initial vibrational level. DR observations at low collision energies ($\lesssim 100$ meV) have turned out to be highly sensitive to small populations in vibrationally excited states. Although ^{3}He ^{4}He$^+$ is radiatively active, which should result in negligible populations in vibrationally excited states after already a few seconds of storage, evidence for stationary, nonthermal populations on vibrational excited levels with fractions of 0.1–1 % was found by analyzing the DR fragment imaging distributions. Pump-probe-type measurements involving switching or variations of the energy of the electron beam allowed the vibrational excitation by energetic electron-ion collisions to be distinguished from that by ion collisions with the residual gas, finding the latter to dominate in the normal storage conditions.

On the longer time scales typical for the evolution of rotational level populations, the presence of the velocity-matched electron beam is seen to cause significant changes of the observed (state-averaged) zero-energy DR rate coefficient, which are attributed to rotational cooling of the ^{3}He ^{4}He$^+$ ions in connection with a dependendence of the

DR cross section on their initial rotational state. The cooling effect could be unambiguously attributed to rotational de-excitation in inelastic low-energy electron-ion collisions. Selective depletion by a rotationally sensitive loss process can be excluded since the only process which could provide for such a sensitivity is low-energy DR, and the corresponding rate coefficient is observed to be two orders of magnitude too low to account for sufficient rotational population changes.

With the developed understanding of the beam dynamics and the contributions of different reaction channels to the DR fragment imaging distribution, an absolute DR rate coefficient of $(7.3 \pm 2.1) \times 10^{-10}$ cm^{3}s^{-1} could be determined for $v=0$ ^{3}He ^{4}He$^+$ ions, referring to an electron thermal energy near 10 meV and to a rotational temperature likely to be near 300 K or below. The result is somewhat larger than predicted in recent theoretical calculations [10] and consistent with earlier experimental limits [12]. Also branching ratios for the four accessible final atomic states could be determined (Table II); they significantly differ from those expected [10] on the basis of the relative importance of the various dissociative potential curves and their diabatic correlations to final atomic levels.

In an energy range up to 40 eV, the energy dependences of the cross sections for DR, DE, and electron-impact vibrational excitation were measured. The DR cross section shows the expected broad peak at ~ 7.3 eV and interesting structures, one of them narrow, at higher energies, which appear to carry detailed information about higher-lying doubly excited states of He$_2$ and call for further investigations. The measurements also reveal the competition between different stabilization pathways after the resonant capture of an electron on He$_2^+$ at energies of several eV.

In a broader view, the results presented in this paper illustrate some of the challenges faced by storage ring experiments setting out to measure very small DR cross sections or to obtain sensitivity on initial rotational states in such measurements. At the present stage, in particular the rotational excitation can only be extracted by indirect conclusions bringing together several experimental findings. In the future, more direct diagnostic techniques to study the rotational population of the stored and electron cooled ion beams, similar to the laser technique demonstrated earlier for a specific case [51], are highly desirable. With such diagnostic techniques established, the strong rotational excitation and de-excitation that appears to be possible by low-energy collisions in the merged electron beam could also be used to actively manipulate the rotational populations in a stored ion beam.

[1] D. R. Bates, Adv. At., Mol., Opt. Phys. **34**, 427 (1994).

[2] M. Larsson, Annu. Rev. Phys. Chem. **48**, 151 (1997).

[3] D. Kella, L. Vejby-Christensen, P. J. Johnson, H. B. Pedersen, and L. H. Andersen, Science **276**, 1530 (1997).

[4] S. L. Guberman, Science **278**, 1276 (1997).

[5] L. Vejby-Christensen, D. Kella, H. B. Pedersen, and L. H. Andersen, Phys. Rev. A **57**, 3627 (1998).

[6] H. Sun and H. Nakamura, J. Chem. Phys. **93**, 6491 (1990).

[7] D. R. Bates, Phys. Rev. **77**, 718 (1950).

[8] V. Kokoouline and C. H. Greene, Phys. Rev. A **68**, 012703 (2003).

[9] R. S. Mulliken, Phys. Rev. **136**, A962 (1964).

[10] L. Carata, A. E. Orel, and A. Suzor-Weiner, Phys. Rev. A **59**, 2804 (1999).

[11] P. C. Stancil, S. Lepp, and A. Dalgarno, Astrophys. J. **509**, 1 (1998).

[12] R. Deloche, P. Monchicourt, M. Cheret, and F. Lampert, Phys. Rev. A **13**, 1140 (1976).

[13] A. V. Phelps and S. C. Brown, Phys. Rev. **86**, 102 (1952).

[14] J. A. Hornbeck and J. P. Molnar, Phys. Rev. **84**, 621 (1951).

[15] X. Urbain, in *Proceedings of the 1999 Conference on Dissociative Recombination, Theory, Experiment and Applications IV*, edited by M. Larsson, L. B. A. Mitchell, and I. F. Schneider (World Scientific, Singapore, 1999), p. 160.

[16] M. Cheret and F. Lampert, C.R. Seances Acad. Sci., Ser. A **275**, 77 (1972).

[17] M. A. Biondi and S. C. Brown, Phys. Rev. **75**, 1697 (1949).

[18] V. A. Ivanov, N. P. Penkin, and Y. E. Skoblo, Opt. Spectrosc. **54**, 552 (1983) [Opt. Spektrosk. **54**, 927 (1983)].

[19] V. A. Ivanov and Y. E. Skoblo, Opt. Spectrosc. **65**, 445 (1989) [Opt. Spektrosk. **65**, 750 (1989).

[20] W. Cencek and J. Rychlewski, J. Chem. Phys. **102**, 2533 (1995).

[21] J. Ackermann and H. Hogreve, Chem. Phys. **157**, 75 (1991).

[22] J. G. Maas, N. P. F. B. van Asselt, P. J. C. M. Nowak, J. Los, S. D. Peyerimhoff, and R. J. Buenker, Chem. Phys. **17**, 217 (1976).

[23] J. P. Flamme, T. Mark, and J. Los, Chem. Phys. Lett. **75**, 419 (1980).

[24] N. Yu and W. H. Wing, Phys. Rev. Lett. **59**, 2055 (1987).

[25] L. Coman, M. Guna, L. Simons, and K. A. Hardy, Phys. Rev. Lett. **83**, 2715 (1999).

[26] W. J. van der Zande and W. Ubachs, Phys. Rev. Lett. **84**, 3212 (2000).

[27] K. Hardy and X. W. Wang, Phys. Rev. Lett. **84**, 3213 (2000).

[28] J. S. Cohen, Phys. Rev. A **13**, 86 (1976).

[29] S. L. Guberman, in *Physics of Ion-Ion and Electron-Ion Collisions, Vol. 83 of NATO Advanced Study Institute Series B: Physics*, edited by F. Brouillard and J. W. McGowan (Plenum, New York, 1983), p. 167.

[30] D. Habs *et al.*, Nucl. Instrum. Methods Phys. Res. B **43**, 390 (1989).

[31] X. Urbain, C. P. Safvan, M. J. Jensen, and L. H. Andersen, in *Proceedings of the 1999 Conference on Dissociative Recombination, Theory, Experiment and Applications IV*, edited by M. Larson, L. B. A. Mitchell, and I. F. Schneider (World Scientific, Singapore, 1999), p. 261.

[32] G. Kilgus, D. Habs, D. Schwalm, A. Wolf, N. R. Badnell, and A. Müller, Phys. Rev. A **46**, 5730 (1992).

[33] Z. Amitay, D. Zajfman, P. Forck, U. Hechtfischer, B. Seidel, M. Grieser, D. Habs, R. Repnow, D. Schwalm, and A. Wolf, Phys. Rev. A **54**, 4032 (1996).

[34] A. Al-Khalili, S. Rosén, H. Danared, A. M. Derkatch, A. Källberg, M. Larsson, A. Le Padellec, A. Neau, J. Semaniak, R. Thomas, M. af Ugglas, L. Vikor, W. Zong, W. J. van der Zande, X. Urbain, M. J. Jensen, R. C. Bilodeau, O. Heber, H. B. Pedersen, C. P. Safvan, L. H. Andersen, M. Lange, J. Levin, G. Gwinner, L. Knoll, M. Scheffel, D. Schwalm, R. Wester, D. Zajfman, and A. Wolf, Phys. Rev. A **68**, 042702 (2003).

[35] R. Wester *et al.*, Nucl. Instrum. Methods Phys. Res. A **413**, 379 (1998).

[36] Z. Amitay, A. Baer, M. Dahan, J. Levin, Z. Vager, D. Zajfman, L. Knoll, M. Lange, D. Schwalm, R. Wester, A. Wolf, I. F. Schneider, and A. Suzor-Weiner, Phys. Rev. A **60**, 3769 (1999).

[37] T. S. Green, Rep. Prog. Phys. **37**, 1257 (1974).

[38] M. Grieser, H. Deitinghoff, D. Habs, R. von Hahn, E. Jaeschke, C.-M. Kleffner, V. Kössler, S. Papureanu, R. Repnow, M.-H. Rhee, D. Schwalm, and A. Schempp, Nucl. Instrum. Methods Phys. Res. A **328**, 160 (1993).

[39] R. von Hahn, M. Grieser, D. Habs, E. Jaeschke, C.-M. Kleffner, J. Liebmann, S. Papureanu, R. Repnow, D. Schwalm, and M. Stampfer, Nucl. Instrum. Methods Phys. Res. A **328**, 270 (1993).

[40] M. Steck, G. Bisoffi, M. Blum, A. Friedrich, C. Geyer, M. Grieser, B. Holzer, E. Jaeschke, M. Jung, D. Krämer, K. Matl, W. Ott, and R. Repnow, Nucl. Instrum. Methods Phys. Res. A **287**, 324 (1990).

[41] S. Pastuszka, U. Schramm, M. Grieser, C. Broude, R. Grimm, D. Habs, J. Kenntner, H.-J. Miesner, T. Schüssler, D. Schwalm, and A. Wolf, Nucl. Instrum. Methods Phys. Res. A **369**, 11 (1996).

[42] H. Poth, Phys. Rep. **196**, 135 (1990).

[43] A. Lampert, A. Wolf, D. Habs, J. Kenntner, G. Kilgus, D. Schwalm, M. S. Pindzola, and N. R. Badnell, Phys. Rev. A **53**, 1413 (1996).

[44] Z. Amitay, D. Zajfman, and P. Forck, Phys. Rev. A **50**, 2304 (1994).

[45] The dipole moment function in Eq. (5) of Ref. [44] was divided by 2, consistent with the derivation in F. O. Ellison J. Chem. Phys. **36**, 478 (1962).

[46] G. Herzberg, *Spectra of Diatomic Molecules* (Van Nostrand, New York, 1950), Chap. V. 3, pp. 208 and 250.

[47] D. Zajfman, S. Krohn, M. Lange, H. Kreckel, L. Lammich, D. Strasser, D. Schwalm, X. Urbain, and A. Wolf, Nucl. Instrum. Methods Phys. Res. B **205**, 360 (2003).

[48] L. Lammich, D. Strasser, H. Kreckel, M. Lange, H. B. Pedersen, S. Altevogt, V. Andrianarijaona, H. Buhr, O. Heber, P. Witte, D. Schwalm, A. Wolf, and D. Zajfman, Phys. Rev. Lett. **91**, 143201 (2003).

[49] T. Tanabe, H. Takagi, I. Katayama, K. Chida, T. Watanabe, Y. Arakaki, Y. Haruyama, M. Saito, I. Nomura, T. Honma, N. Noda, and K. Hosono, Phys. Rev. Lett. **83**, 2163 (1999).

[50] S. Krohn, Z. Amitay, A. Baer, D. Zajfman, M. Lange, L. Knoll, J. Levin, D. Schwalm, R. Wester, and A. Wolf, Phys. Rev. A **62**, 032713 (2000).

[51] U. Hechtfischer, Z. Amitay, P. Forck, M. Lange, J. Linkemann, M. Schmitt, U. Schramm, D. Schwalm, R. Wester, D. Zajfman, and A. Wolf., Phys. Rev. Lett. **80**, 2809 (1998).

[52] M. Lange *et al.* (unpublished); M. Lange, Ph.D. thesis, Uni-

versity of Heidelberg, 2001 (http://www.ub.uni-heidelberg.de/archiv/1774).

[53] K. Nakashima, H. Takagi, and H. Nakamura, J. Chem. Phys. **86**, 726 (1986).

[54] I. Rabadan, S. K. Sarpal, and J. Tennyson, Mon. Not. R. Astron. Soc. **299**, 171 (1998).

[55] I. Rabadan, S. K. Sarpal, and J. Tennyson, J. Phys. B **31**, 2077 (1998).

[56] A. Faure and J. Tennyson, Mon. Not. R. Astron. Soc. **325**, 443 (2001).

[57] Z. Vager, R. Naaman, and E. P. Kanter, Science **244**, 426 (1989).

[58] D. Zajfman, Comments At. Mol. Phys. **29**, 369 (1994).

[59] D. Zajfman, T. Graber, E. P. Kanter, and Z. Vager, Phys. Rev. A **46**, 194 (1992).

[60] R. Garcia-Molina, C. D. Denton, I. Abril, and N. R. Arista, Phys. Rev. A **62**, 012901 (2000).

[61] L. Lammich, H. Buhr, H. Kreckel, S. Krohn, M. Lange, D. Schwalm, R. Wester, A. Wolf, D. Strasser, D. Zajfman, Z. Vager, I. Abril, S. Heredia-Avalos, and R. Garcia-Molina, Phys. Rev. A **69**, 062904 (2004).

[62] P. Forck, C. Broude, M. Grieser, D. Habs, J. Kenntner, J. Liebmann, R. Repnow, D. Schwalm, A. Wolf, Z. Amitay, and D. Zajfman, Phys. Rev. Lett. **72**, 2002 (1994).

[63] A. E. Orel and K. C. Kulander, Phys. Rev. A **54**, 4992 (1996).

[64] X. Urbain, N. Djurić, C. P. Safvan, M. J. Jensen, H. B. Pedersen, L. Vejby Søgaard, and L. H. Andersen, J. Phys. B **38**, 43 (2005).

[65] J. Royal and A. E. Orel, in *Proc. 6th Int. Conf. on Dissociative Recombination, Theory, Experiments and Applications, Mosbach, Germany, 2004* J. Phys. Conf. Series 4, 177 (2004).

[66] S. L. Guberman, Phys. Rev. A **49**, R4277 (1994).

[67] B. K. Sarpal, J. Tennyson, and T. A. Morgan, J. Phys. B **27**, 5943 (1994).

[68] J. Semaniak, S. Rosén, G. Sundström, C. Strömholm, S. Datz, H. Danared, M. af Ugglas, M. Larsson, W. J. van der Zande, Z. Amitay, U. Hechtfischer, M. Grieser, R. Repnow, M. Schmidt, D. Schwalm, R. Wester, A. Wolf, and D. Zajfman, Phys. Rev. A **54**, R4617 (1996).

[69] S. Krohn, M. Lange, M. Grieser, L. Knoll, H. Kreckel, J. Levin, R. Repnow, D. Schwalm, R. Wester, P. Witte, A. Wolf, and D. Zajfman, Phys. Rev. Lett. **86**, 4005 (2001).